Libration-driven multipolar instabilities

D. Cébron[1,†], **S. Vantieghem**[1] **and W. Herreman**[2]

[1]Institut für Geophysik, Sonneggstrasse 5, ETH Zürich, CH-8092 Zürich, Switzerland

[2]Université de Paris-Sud (LIMSI-CNRS), BP 133, F-91403 Orsay CEDEX, France

We consider rotating flows in non-axisymmetric enclosures that are driven by libration, i.e. by a small periodic modulation of the rotation rate. Thanks to its simplicity, this model is relevant to various contexts, from industrial containers (with small oscillations of the rotation rate) to fluid layers of terrestrial planets (with length-of-day variations). Assuming a multipolar n-fold boundary deformation, we first obtain the two-dimensional basic flow. We then perform a short-wavelength local stability analysis of the basic flow, showing that an instability may occur in three dimensions. We christen it the libration-driven multipolar instability (LDMI). The growth rates of the LDMI are computed by a Floquet analysis in a systematic way, and compared to analytical expressions obtained by perturbation methods. We then focus on the simplest geometry allowing the LDMI, a librating deformed cylinder. To take into account viscous and confinement effects, we perform a global stability analysis, which shows that the LDMI results from a parametric resonance of inertial modes. Performing numerical simulations of this librating cylinder, we confirm that the basic flow is indeed established and report the first numerical evidence of the LDMI. Numerical results, in excellent agreement with the stability results, are used to explore the nonlinear regime of the instability (amplitude and viscous dissipation of the driven flow). We finally provide an example of LDMI in a deformed spherical container to show that the instability mechanism is generic. Our results show that the previously studied libration-driven elliptical instability simply corresponds to the particular case $n = 2$ of a wider class of instabilities. Summarizing, this work shows that any oscillating non-axisymmetric container in rotation may excite intermittent, space-filling LDMI flows, and this instability should thus be easy to observe experimentally.

Key words: parametric instability, rotating flows, topographic effects

1. Introduction

It is basic planetary and astrophysical knowledge that celestial objects are rapidly rotating and orbit around each other. This combination of rapid rotation and mutual gravitational interaction forces these objects to synchronize, get phase-locked, precess, librate and be tidally deformed. Since the pioneering work of Poincaré (1910), there

† Email address for correspondence: dcebron@gmail.com

has been interest in modelling how the liquid parts of such rotating objects can respond to this precession, libration and tidal deformations. In this work, we combine both effects of longitudinal libration and deformations by considering the ideal case of a deformed rotating rigid container that undergoes a periodic modulation of its rotation rate. The simplicity of this ideal model makes it relevant to various contexts, from industrial rotating fluid containers to planetary fluid layers. To understand the specific details of this study, we give below a short review on previous relevant studies on both ingredients, i.e. librations and deformed containers.

1.1. *Libration-driven flows*

Librations can be decomposed in two classes: longitudinal and latitudinal libration. In the first case, the rotation speed of the object oscillates around some mean value, but the planet continues to rotate about the same axis. The case of latitudinal libration is more complex, as it is the figure axes of the object that oscillate about some mean direction. In most cases, persistent librations are due to gravitational coupling between an astrophysical body and its main gravitational partner around which it orbits (Comstock & Bills 2003), but they can also be due to exchange of angular momentum between the solid mantle of a planet and its atmosphere, as on Titan. On the Earth, the change in polar ice sheets, between ice and non-ice ages, modifies the inertia tensor of the Earth, which leads to oscillations of the mantle rotation rate (see e.g. Miyagoshi & Hamano (2013), where the consequences on the Earth's magnetic field are discussed). Note that these oscillations are called length-of-day (LOD) variations, rather than libration, for non-synchronized planets like the Earth. Finally, strong enough meteorite impacts may be responsible for the occurrence of transient decaying libration movements (Wieczorek & Le Feuvre 2009; Le Bars *et al.* 2011). The analysis of the librations of a planet allows one to define constraints on its internal structure (e.g. Margot *et al.* (2007) explain Mercury's longitudinal libration by the presence of a liquid core). The main problem of these models is that they presuppose that the fluid rotates without being disturbed by the libration of the solid shell, except in a thin viscous boundary layer, the Ekman layer, at the solid–liquid interface. This is not a valid approximation in many cases, and the non-rigid response of the fluid in the liquid layer of the planet has thus to be characterized.

Because of the astrophysical applications of libration-driven flows, a number of studies have been devoted to librating axisymmetric containers in order to investigate the role of the viscous coupling. It has been shown that longitudinal libration in axisymmetric containers can drive inertial waves in the bulk of the fluid as well as boundary-layer centrifugal instabilities in the form of Taylor–Görtler rolls (Aldridge 1967, 1975; Aldridge & Toomre 1969; Tilgner 1999; Noir *et al.* 2009; Calkins *et al.* 2010; Sauret *et al.* 2012). In addition, laboratory and numerical studies have corroborated the analytically predicted generation of a mainly retrograde axisymmetric and stationary zonal flow in the bulk, based upon nonlinear interactions within the Ekman boundary layers (Wang 1970; Busse 2010*a*,*b*; Calkins *et al.* 2010; Noir *et al.* 2010, 2012; Sauret *et al.* 2010, 2012; Sauret & Le Dizès 2013).

Although it is practicable to isolate the effect of viscous coupling, the spherical approximation of the core–mantle or ice shell–subsurface ocean boundaries is not fully accurate from a planetary point of view and is very restrictive from a fluid dynamics standpoint. Indeed, owing to the rotation of the planet and the gravitational interactions with companion bodies, the general shape of the core–mantle boundary can differ significantly from that of a sphere. In this article, we precisely study the impact of the combination of libration and boundary deformations.

1.2. *Elliptical and multipolar instabilities*

The effect of boundary deformations on rotating flows has been carefully studied in the case of tidal deformations. It is recognized that tides generate flows in the mantle that may dissipate enough energy to lead to a synchronization. Since Malkus' experiments (Malkus 1989), research into the impact of tides on liquid planetary interiors has been ongoing and it has been quite actively studied in recent years. Most previous studies consider the case of an elliptically deformed container, with a constant, non-zero differential rotation between the fluid and the elliptical distortion. In a geophysical context, this corresponds to a non-synchronized body with a constant spin rate Ω_0, subject to dynamical tides rotating at the constant orbital rotation rate Ω_{orb} (i.e. the axes of the core–mantle boundary (CMB) elliptical deformation rotates at Ω_{orb}). In this case, the elliptical streamlines of the two-dimensional (2D) basic flow can be destabilized into a fully three-dimensional (3D) flow by an elliptical instability, the so-called tidally driven elliptical instability (TDEI) (see e.g. Kerswell 2002).

Generally speaking, an elliptical instability can be seen as an inherent local instability due to the non-zero strain of elliptical streamlines (Bayly 1986; Waleffe 1990), or as a parametric resonance between two free inertial waves (respectively, modes) of a rotating unbounded (respectively, bounded) fluid and an elliptical strain, which is not an inertial wave or mode (Moore & Saffman 1975; Tsai & Widnall 1976). Such a resonance mechanism, confirmed by numerous works in elliptically deformed cylinders (e.g. Eloy, Le Gal & Le Dizès 2000, 2003; Eloy & Le Dizès 2001; Guimbard *et al.* 2010; Lavorel & Le Bars 2010) and ellipsoids (Lacaze, Le Gal & Le Dizès 2004, 2005; Le Bars, Le Dizès & Le Gal 2007; Le Bars *et al.* 2010; Cébron *et al.* 2010*a*; Cébron, Le Bars & Meunier 2010*b*; Cébron, Maubert & Le Bars 2010*c*), is not limited to elliptical deformation but also operates for a general *n*-fold deformation (Le Dizès & Eloy 1999). The elliptical instability is thus a particular case of a wider class of instability, the multipolar instability, which can also be seen as an inherent local instability of the multipolar streamlines (Le Dizès & Eloy 1999; Le Dizès 2000), or as a parametric resonance between two free inertial waves (respectively, modes) of the rotating unbounded (respectively, bounded) fluid and an *n*-fold strain (Eloy & Le Dizès 2001; Eloy *et al.* 2003).

1.3. *Libration-driven multipolar instabilities (LDMI)*

According to Le Dizès (2000), who considers the case of a constant non-zero differential rotation between the fluid and the multipolar distortion, the multipolar instability vanishes in the case of synchronous rotation ($\Omega_0 = \Omega_{orb}$). However, in the very particular case of elliptical deformation, Cébron *et al.* (2012*a,c*) have recently numerically and experimentally confirmed that oscillations around this synchronous state are sufficient to excite elliptical instability, the so-called libration-driven elliptical instability (LDEI), as previously suggested by previous local stability studies of unbounded inviscid flows (Kerswell & Malkus 1998; Herreman, Le Bars & Le Gal 2009; Cébron *et al.* 2012*b*). The results obtained by Wu & Roberts (2013) in a spheroid are in agreement with these studies: by considering a particular class of perturbations that satisfy the non-penetration boundary conditions and volume conservation, they show that an instability is possible, and they confirm this result with simulations. This could be of fundamental importance in planetary liquid cores and subsurface oceans of synchronized bodies, where librations are generically present (e.g. Le Bars *et al.* 2011; Noir *et al.* 2012).

In this work, we aim to show that this result holds for a general multipolar deformation, which leads us to consider the LDEI as a particular case of a wider
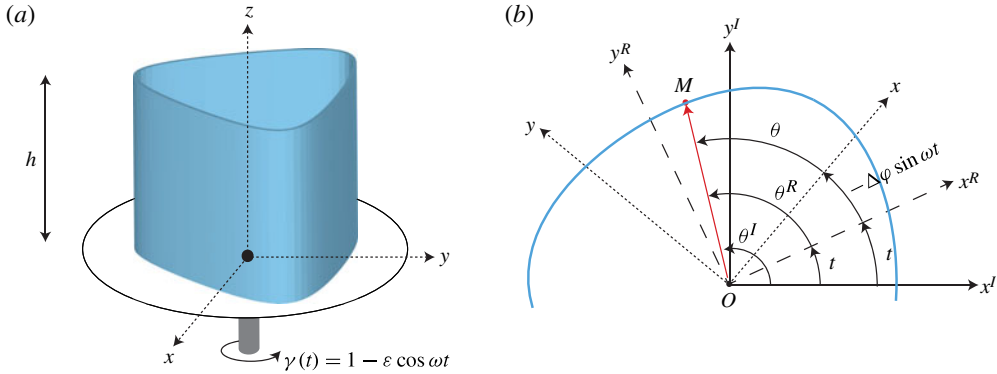
FIGURE 1. (Colour online) (*a*) Sketch of the studied set-up. A deformed cylinder is put on a turntable that rotates at the dimensionless rotation speed $\gamma(t) = 1 - \varepsilon \cos \omega t$. The combination of libration and deformation drives a 2D basic flow, which can be destabilized into 3D flows through the LDMI. (*b*) Different frames of reference are used: the librating frame (x, y, θ; no superscript) attached to the turntable, the inertial (or laboratory) frame (x^I, y^I, θ^I) and the frame rotating at constant speed 1 (x^R, y^R, θ^R).

class of instabilities, the LDMI. To do so, this work is organized as follows. In § 2, we define the problem and the considered basic flow. Then, in § 3 we perform various theoretical stability analyses of the basic flow: considering unbounded inviscid flows, we first generalize previous local analysis to an arbitrary multipolar flow (§ 3.1), and then we take into account viscosity and confinement effects in a cylinder by developing the first eigenmodes global stability analysis of libration-driven flows (§ 3.2). In § 4, we finally compare our theoretical predictions with 3D nonlinear viscous simulations and explore the nonlinear regime using a home-made massively parallel finite-volume code.

2. Problem definition

2.1. *Dimensionless equations*

In this article, we consider a fluid contained in a librating and deformed rigid cylinder as sketched in figure 1(*a*). In dimensional form, the librating frame of reference (x, y, z) rotates at variable speed $\Omega_0 \gamma(t) e_z$ with respect to the inertial frame of reference (superscript I; see figure 1*b*), where Ω_0 is the time-averaged rotation rate. Using $1/\Omega_0$ as the time scale, we write the dimensionless rotation speed $\gamma(t)$ as (see figure 1)

$$\gamma(t) = \frac{\mathrm{d}}{\mathrm{d}t}(t - \Delta\varphi \sin \omega t) = 1 - \varepsilon \cos \omega t, \qquad (2.1)$$

and call ω the libration frequency, $\Delta\varphi$ the libration angle and $\varepsilon = \omega \Delta\varphi$ the libration amplitude. The fluid container is immobile in the librating frame (which rotates at $\gamma(t)$). It takes the form of a deformed cylinder limited by two horizontal boundaries at $z = 0$, $z = h$, and a lateral wall located at, in cylindrical coordinates (r, θ, z),

$$\zeta(r, \theta) = C + \tfrac{1}{2} = 0, \qquad (2.2)$$

where

$$C = -\frac{r^2}{2} + p\frac{r^n}{n}\cos n\theta \qquad (2.3)$$

defines a multipolar deformation (e.g. Le Dizès & Eloy 1999). Note that, in the limit of small deformations $p \ll 1$, an explicit solution of $\zeta(r, \theta) = 0$, i.e. of the lateral wall location, is given by

$$r = 1 + \frac{p}{n}\cos n\theta + O(p^2). \qquad (2.4)$$

The coordinates r, z and the container height h are scaled in units of R, the radius of the undeformed cylindrical container. We will denote by p the amplitude of the multipolar deformation. The integer n sets the type (or order) of the multipolar deformation of the boundary: $n = 2$ for elliptical deformation, $n = 3$ for tripolar deformation, $n \in \mathbb{N}$ for a general n-fold deformation.

Considering a Newtonian incompressible fluid with constant and homogeneous material properties, the combination of libration and deformation induces flows governed by the Navier–Stokes and mass conservation equations. Using $1/\Omega_0$ as the time scale and $\Omega_0 R$ for the velocity scale, these equations can be written in the librating frame of reference as

$$\frac{\partial \boldsymbol{u}}{\partial t} + (\boldsymbol{u} \cdot \nabla)\boldsymbol{u} = -\nabla \Pi + E\nabla^2 \boldsymbol{u} - 2\gamma \boldsymbol{e}_z \times \boldsymbol{u} - \frac{d\gamma}{dt}\boldsymbol{e}_z \times \boldsymbol{x}, \qquad (2.5)$$

$$\nabla \cdot \boldsymbol{u} = 0, \qquad (2.6)$$

where $E = \nu/(\Omega_0 R^2)$ is the Ekman number, with ν the fluid kinematic viscosity, $\boldsymbol{u}$ the velocity of the fluid in the librating frame and Π the reduced pressure taking the centrifugal force into account. On the lateral boundary, we consider no-slip boundary conditions, i.e. $\boldsymbol{u}(\zeta = 0) = \boldsymbol{0}$, and the top and bottom are periodic boundaries, i.e.

$$\boldsymbol{u}|_{z=0} = \boldsymbol{u}|_{z=h} \quad \text{and} \quad \left.\frac{\partial \boldsymbol{u}}{\partial z}\right|_{z=0} = \left.\frac{\partial \boldsymbol{u}}{\partial z}\right|_{z=h}. \qquad (2.7)$$

We thus allow for a mean axial flow to exist.

2.2. *Two-dimensional inviscid basic flow*

In the inviscid limit $E = 0$, one can find a 2D basic flow $\boldsymbol{u} = \boldsymbol{U}$ that exactly satisfies the previous equations (2.5) and (2.6):

$$\boldsymbol{U} = \nabla \times (\Psi \boldsymbol{e}_z), \quad \Psi = C(r, \theta)\,\varepsilon \cos \omega t = \left(-\frac{r^2}{2} + p\frac{r^n}{n}\cos n\theta\right)\varepsilon \cos \omega t. \qquad (2.8)$$

Taking the axial component of the curl of (2.5), the equation for axial vorticity reduces to

$$\frac{d(\nabla^2 \Psi)}{dt} = 2\frac{d\gamma}{dt}, \qquad (2.9)$$

which is exactly satisfied. We also see that the basic flow is always parallel to that boundary, so that the inviscid boundary condition $\boldsymbol{U} \cdot \boldsymbol{e}_n = \boldsymbol{0}|_{\zeta=0}$ is also satisfied (where $\boldsymbol{e}_n$ is the outward boundary normal unit vector). Moreover, owing to the separation of the space and time variables in the streamfunction (2.8) of our 2D basic flow, each fluid particle, as seen from the librating frame, oscillates back and forth along a part
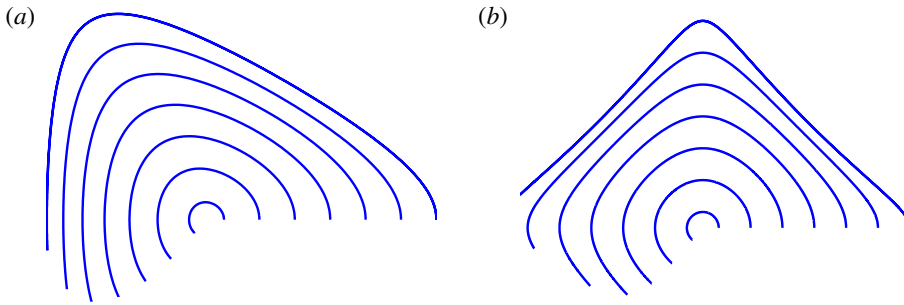
(a)   (b)

FIGURE 2. (Colour online) Pathlines of the multipolar flow (2.8) for a libration angle $\Delta\varphi = 2$, a deformation $p = 0.45$, with initial positions given by $\theta_{(t=0)} = 0$ and an initial radius from $r_{(t=0)} = 0.1$ to $r_{(t=0)} = 1.3$ with steps of 0.2. (a) For $n = 3$. Here, (C, β_3) varies between $(C, \beta_3) = (-0.0049, 0.0768)$, reached for $r_{(t=0)} = 0.1$, and $(C, \beta_3) = (-0.5155, 0.7914)$, reached for $r_{(t=0)} = 0.8$. (b) For $n = 4$. Here, (C, β_4) varies between $(C, \beta_4) = (-0.005, 0.009)$, reached for $r_{(t=0)} = 0.1$, and $(C, \beta_4) = (-0.2739, 0.9426)$, reached for $r_{(t=0)} = 0.8$.

of a streamline $C = \text{const.}$ Thus, any streamline $C = \text{const.}$ does not change with time, and the pathlines of any particle located on this streamline at $t = 0$ are thus part of this streamline. This behaviour is illustrated in figure 2, which shows several pathlines in the librating frame, for $n = 3, 4$. The particles follow a track $C = \text{const.}$ and join their initial position after completing a periodic cycle. Following Le Dizès & Eloy (1999), we introduce the parameter

$$\beta_n = p\left(\frac{2n|C|}{n-2}\right)^{n/2-1}, \tag{2.10}$$

which measures the local asymmetry of the streamlines (and pathlines) and varies in $\beta_n \in [0; 1]$. For $n = 2$, the flow is a uniform elliptical flow and all the pathlines have the same $\beta_2 = p$ that can be identified with the ellipticity ($\beta_2 = |1 - \Upsilon^2|/(1 + \Upsilon^2)$ with Υ the axes ratio). For $n \geqslant 3$, β_n varies with C and the flow is thus not uniform. As β_n is increased, the streamlines become more and more angular, exhibiting n singular points (corners) for $\beta_n = 1$. For $\beta_n > 1$, the streamlines of an unbounded flow are no longer closed, and our analysis will thus be restricted to the range $\beta_n \in [0; 1]$. Note that the maximum value p_{max} for p, reached when $\beta_n = 1$ on the boundary streamline $\zeta(r, \theta) = 0$, i.e. $C = -1/2$, decreases with n, tending towards an asymptotic constant value $p_{max} = e^{-1}$ when n becomes infinite (with $e = \exp 1$).

2.3. *Libration as seen from other frames*

The librating frame is best adapted for numerical simulations, since the boundary has a fixed shape, but the local stability theory will be formulated in the inertial frame (superscript I) to avoid any inertial fictitious force, and the global theory in the frame rotating at constant speed $\Omega_0 e_z$ (superscript R). The different reference frames are illustrated in figure 1(b). We can relate the azimuthal angles $\theta, \theta^I, \theta^R$ in the three frames by

$$\theta^I = \theta^R + t = \theta + t - \Delta\varphi \sin \omega t. \tag{2.11}$$

Parameter	Name	Range for the simulations
ω	Libration frequency	2–4.5
ε	Libration amplitude	0.8–1.5
$\gamma(t)\boldsymbol{e}_z = [1 - \varepsilon \cos \omega t]\boldsymbol{e}_z$	Rotation vector	—
p	Multipolar deformation amplitude	0.2–0.5
n	Multipolar deformation order	3
h	Height of the cylinder	2
$E = \nu/(\Omega_0 R^2)$	Ekman number	10^{-4}–1.5×10^{-3}
C	Streamfunction spatial dependence	—
$\beta_n = p\left(\dfrac{2n|C|}{n-2}\right)^{n/2-1}$	Local pathline/streamline deformation	0–$\sqrt{3}/2$

TABLE 1. Dimensionless control parameters involved in the problem definition.

Flows in the different frames are related as

$$\boldsymbol{u}^I = \boldsymbol{u}(r, \theta^I - t + \Delta\varphi \sin \omega t, z, t) + (1 - \varepsilon \cos \omega t)\,\boldsymbol{e}_z \times \boldsymbol{x}^I, \qquad (2.12a)$$

$$\boldsymbol{u}^R = \boldsymbol{u}(r, \theta^R + \Delta\varphi \sin \omega t, z, t) - \varepsilon \cos \omega t\,\boldsymbol{e}_z \times \boldsymbol{x}^R. \qquad (2.12b)$$

It is instructive to see that the basic flow takes a particularly simple, potential form in the rotating frame of reference,

$$\boldsymbol{U}^R = \boldsymbol{\nabla}\left[-\varepsilon p \frac{r^n}{n} \cos \omega t \sin n(\theta^R + \Delta\varphi \sin \omega t)\right]. \qquad (2.13)$$

This clearly shows that the boundary deformations

$$\zeta^R(r, \theta^R, t) = \frac{1}{2} - \frac{r^2}{2} + p\frac{r^n}{n} \cos n(\theta^R + \Delta\varphi \sin \omega t) = 0 \qquad (2.14)$$

induce an $O(\varepsilon p)$ potential flow, stretching some directions, but compressing others. The transverse stretching allows the basic flow to destabilize inertial modes with a horizontal vorticity aligned with the stretched axis, exactly as in the case of elliptical instability (Waleffe 1990). The specifics of the librational forcing are related to the broader frequency content of the boundary deformation and basic flow. This can be seen by expanding the functions appearing in rotating frame expressions of the basic flow and the boundary deformation:

$$\cos \omega t \cos n(\theta + \Delta\varphi \sin \omega t) = e^{in\theta}f(t) + \text{c.c.}, \qquad (2.15)$$

$$\cos n(\theta + \Delta\varphi \sin \omega t) = e^{in\theta}g(t) + \text{c.c.}, \qquad (2.16)$$

where c.c. is as usual the complex conjugate, and

$$f(t) = \frac{1}{4} \sum_{j \in \mathbb{Z}} [\mathrm{J}_{j-1}(n\Delta\varphi) + \mathrm{J}_{j+1}(n\Delta\varphi)]\, e^{ij\omega t}, \qquad (2.17)$$

$$g(t) = \frac{1}{2} \sum_{j \in \mathbb{Z}} \mathrm{J}_j(n\Delta\varphi)\, e^{ij\omega t}, \qquad (2.18)$$

with J_j denoting Bessel functions of the first kind (see formulae (9.1.42) and (9.1.45) in Abramowitz & Stegun (1964)). For finite angles $\Delta\varphi$, librational forcing involves

	Unbounded	Inviscid $(E = 0)$	Short-wavelength $(\vartheta \ll 1)$	Small forcing $(\varepsilon p \ll 1)$
Problem definition: § 2	—	—	—	—
Local analysis: § 3.1	✓	✓	✓	—
Local analytical analysis: § 3.1.3	✓	✓	✓	✓
Global analysis: § 3.2	—	—	—	✓
Simulations: § 4	—	—	—	—

TABLE 2. Assumptions used in the different sections of this work.

more than one frequency. Any of these various frequency components will be able to couple different inertial modes, and this is the basic feature of LDMI in comparison with previous studies (Le Dizès & Eloy 1999; Le Bars *et al.* 2007).

We denote by f_j and $(f^\dagger)_j$ the coefficient in front of the $\exp(\mathrm{i}j\omega t)$ component of $f(t)$ and its complex conjugate $f^\dagger(t)$, and similarly for g_j and $(g^\dagger)_j$. In the limit of small libration angles $\Delta\varphi \to 0$, there is one dominant frequency in the boundary deformation, as $\mathrm{J}_0(0) = 1$ and $\mathrm{J}_j(0) = 0$ for $j \neq 0$: we have $f(t) \to (\cos\omega t)/2$ and $g(t) \to 1/2$, but as $\Delta\varphi \to 0$, the libration amplitude $\varepsilon \to 0$ for a fixed ω.

3. Linear stability analysis

In this section, we are concerned with the linear instability of the flow (2.8). We will perturb the basic flow U with a small 3D flow u and search to identify the conditions under which u can grow in time. In a local stability analysis, this problem is reduced to a stability study of each basic flow particle trajectory separately. This leads to general formulae that are broadly applicable. In a global analysis, we analyse the system (fluid plus container) as a whole. This leads to precise information on the kind of modes that can be destabilized in a particular fluid domain. Comparing the two approaches will lead to useful insights here. Our purpose is to perform a rigorous study on LDMI that completes previous work on multipolar instability (Le Dizès & Eloy 1999; Eloy & Le Dizès 2001; Eloy *et al.* 2003) and LDEI (Kerswell & Malkus 1998; Herreman *et al.* 2009; Cébron *et al.* 2012*a*,*b*,*c*).

3.1. *Local stability analysis: unbounded flows*

In this section, we investigate the inviscid stability of the pathlines of the basic flow U in a fluid domain assumed to be unbounded (see table 2). To do so, we consider a perturbed solution of the equations of motion under the form of localized plane waves along the pathlines of the basic flow, and we assume that the characteristic wavelength ϑ of the plane waves is very small (short-wavelength hypothesis).

3.1.1. *Short-wavelength Lagrangian stability analysis*

The approach we follow here is based on the short-wavelength Lagrangian theory, used by Bayly (1986) and Craik & Criminale (1986), and then generalized in Friedlander & Vishik (1991), Lifschitz & Hameiri (1991, 1993) and Lifschitz (1994), where the whole theory is thoroughly explained. This theory is now rather classical in stability studies of flows (e.g. Bayly, Holm & Lifschitz 1996; Lebovitz & Lifschitz 1996; Leblanc & Cambon 1997), and we thus only recall below some basic elements of the stability analysis in following the approach of Le Dizès & Eloy (1999). We found it simplest to work in the inertial frame of reference, but the superscript I will be omitted in what follows. The perturbation velocity u is written in the geometrical

optics or Wentzel–Kramers–Brillouin (WKB) form:

$$\boldsymbol{u}(\boldsymbol{x}, t) = \boldsymbol{a}(\boldsymbol{x}, t)e^{i\chi(\boldsymbol{x}, t)/\vartheta}. \tag{3.1}$$

Here, the amplitude $\boldsymbol{a}(\boldsymbol{x}, t)$ and phase $\chi(\boldsymbol{x}, t)$ are real functions dependent on space $\boldsymbol{x}$ and time t. The characteristic wavelength $\vartheta \ll 1$ is the small parameter used for the asymptotic (WKB) expansion. In the inviscid limit, the evolution of (3.1) is governed by the linearized Euler equations. Along the pathlines of $\boldsymbol{U}$, the leading-order problem can be written in Lagrangian form as a system of ordinary differential equations (Lifschitz 1994):

$$\frac{d\boldsymbol{X}}{dt} = \boldsymbol{U}(\boldsymbol{X}, t), \tag{3.2}$$

$$\frac{d\mathcal{K}}{dt} = -(\nabla\boldsymbol{U})^{\mathrm{T}}(\boldsymbol{X}, t)\mathcal{K}, \tag{3.3}$$

$$\frac{d\boldsymbol{a}}{dt} = \left(\frac{2\mathcal{K}\mathcal{K}^{\mathrm{T}}}{|\mathcal{K}|^2} - \boldsymbol{I}\right)\nabla\boldsymbol{U}(\boldsymbol{X}, t)\,\boldsymbol{a}, \tag{3.4}$$

with constraint

$$\mathcal{K} \cdot \boldsymbol{a} = 0. \tag{3.5}$$

Here $d/dt = \partial_t + \boldsymbol{U} \cdot \nabla$ are Lagrangian derivatives, $\boldsymbol{I}$ is the identity matrix and $\mathcal{K} = \nabla\chi$ is the (local) wavevector along the Lagrangian trajectory $\boldsymbol{X}$. The incompressibility condition (3.5) is always fulfilled if the initial condition $(\boldsymbol{X}_0, \mathcal{K}_0, \boldsymbol{a}_0)$ satisfies $\mathcal{K}_0 \cdot \boldsymbol{a}_0 = 0$ (Le Dizès 2000). As shown by Lifschitz & Hameiri (1991), the existence of an unbounded solution for $\boldsymbol{a}$ provides a sufficient condition for instability. Assuming closed pathlines, stability is naturally analysed over one turnover period T along the pathline. Note that this system of equations can be seen as an extension of rapid distortion theory (RDT) to non-homogeneous flows (Cambon, Teissedre & Jeandel 1985; Cambon *et al.* 1994; Sipp & Jacquin 1998).

In practice, (3.2) has to be solved as a first step to know the trajectory $\boldsymbol{X}$ emerging out of initial position $\boldsymbol{X}_0$. Knowing $\boldsymbol{X}$, one can solve the wavevector equation (3.3) for an initial vector $\mathcal{K}_0$. As the magnitude or sign of $\mathcal{K}_0$ cannot influence the growth of $\boldsymbol{a}$, and because $\mathcal{K}_0 \cdot \boldsymbol{a}_0 = 0$ in the particular case of a two-dimensional flow with closed streamlines in the x–y plane, we can consider the role of different $\mathcal{K}_0$ with a single angle

$$\xi = \arccos\left(\frac{\mathcal{K}_0 \cdot \boldsymbol{e}_z}{\|\mathcal{K}_0\|}\right) \tag{3.6}$$

that varies in the interval $\xi \in [0°, 90°]$ (e.g. Le Dizès & Eloy 1999). Knowledge of $\boldsymbol{X}$ and $\mathcal{K}$ finally allows one to solve (3.4) for the amplitudes $\boldsymbol{a}$ and to look for growing solutions. As shown by Lifschitz & Hameiri (1991), the existence of an unbounded time evolution of $\boldsymbol{a}$ provides a sufficient condition for instability. The result holds for viscous flows (Landman & Saffman 1987; Lifschitz & Hameiri 1991) if the characteristic wavelength ϑ is larger than $\sqrt{E/\sigma}$, where σ is the maximum inviscid growth rate of $\|\boldsymbol{a}(\boldsymbol{x}, t)\| \sim \exp(\sigma t)$. Finally, to close this brief description of short-wavelength Lagrangian theory, it is worth mentioning that viscous effects on the perturbations can be easily taken into account by adding to the inviscid growth rate σ the viscous damping rate $-\mathcal{K}^2 E$ (e.g. Craik & Criminale 1986; Landman & Saffman 1987; Le Dizès 2000).
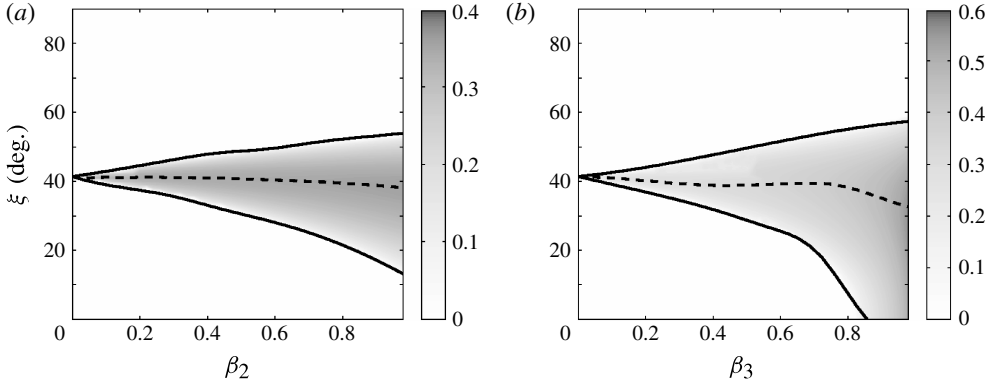
FIGURE 3. Growth rates σ^* in the β_n–ξ plane, obtained from the Floquet analysis, for $\varepsilon = 1.5$ and $\omega = 3$ (as shown in § 3.1.3 in the limit $\varepsilon p \ll 1$, only one tongue exists for $\omega > 2$). The greyscale bar represents σ^*, solid lines are the boundaries of the tongue (corresponding to a non-zero σ^*) and the dashed line represents the values of ξ that maximize σ^*. (a) $n = 2$ (b) $n = 3$.

3.1.2. *Numerical results: Floquet analysis*

We now solve the previous problem in the inertial frame using the basic flow (2.8). As particles always come back to their initial position after a time that can be denoted T, we have periodic trajectories X, which also results in periodic functions $\mathcal{K}$ whatever the chosen $\mathcal{K}_0$. With $\mathcal{K}(t)$ periodic, (3.4) can be analysed in terms of Floquet theory (e.g. Bender & Orszag 1978). Starting from three canonical initial conditions, in matrix form $\boldsymbol{a}(0) = \boldsymbol{I}$, we integrate (3.4) over exactly one period $t \in [0, T]$ to obtain the monodromy matrix $\boldsymbol{a}(T)$. The Floquet exponents are the three eigenvalues ϖ_1, ϖ_2 and ϖ_3 of this matrix and represent the multiplicative gain of the associated Floquet eigenvector, over one period T. As noted by Kerswell (1993*b*), $\det \boldsymbol{a}(T) = 1$, and $\mathcal{K}_0 = \mathcal{K}(0) = \mathcal{K}(T)$ is a left eigenvector of $\boldsymbol{a}(T)$, with an eigenvalue $\varpi_1 = 1$. The two other eigenvalues are then either complex conjugates on the unit circle, indicating stability, or a real, reciprocal pair, one of which lies outside the unit circle. In this last case, an instability is present, with growth rate given by

$$\sigma(n, \varepsilon, \beta_n, \xi) = \frac{1}{T} \ln|\varpi(n, \varepsilon, \beta_n, \xi)|. \tag{3.7}$$

Figure 3 show results from some calculations of σ in the β_n–ξ plane, for fixed $\varepsilon = 1.5$ and $\omega = 3$. We clearly see resonance tongues emerging from a well-defined angle, and we will show in § 3.1.3 that its value is given by $\xi = \arccos(\omega/4)$; here $\xi = 41.41°$. As β_n increases, a broadening band of angles becomes destabilized. If we focus only on the largest growth rate, obtained by maximizing over all angles ξ and rescale it with respect to the local strain rate

$$\sigma^* = \max_{\xi} \frac{\sigma}{\varepsilon p(n-1)|2C|^{n/2-1}}, \tag{3.8}$$

we get the curves of figure 4. For $n = 2$, the rescaled growth rate increases monotonically with the libration magnitude ε and β_n. In the elliptical case $n = 2$, the impact of considering large deformation β_2 remains very small, but in the triangular case $n = 3$, σ^* may double in magnitude and increases very sharply when $\beta_3 \to 1$.
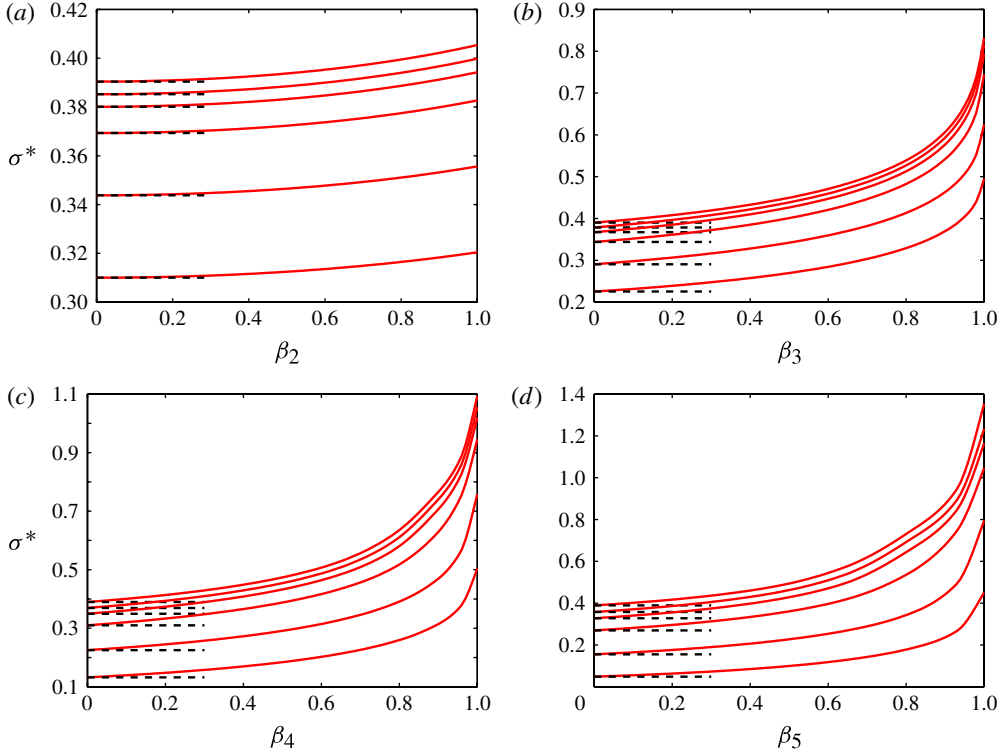
FIGURE 4. (Colour online) Comparison of the analytical growth rate (black dashed lines) given by (3.16), obtained for $\varepsilon p \ll 1$, with the solution (grey solid lines; red online) of stability (3.2)–(3.4) for $\omega = 3$ and $\varepsilon = 0.1, 0.5, 0.7, 1.0, 1.5$ and 2.0 (from the uppermost curve to the lowest one): (*a*) $n = 2$; (*b*) $n = 3$; (*c*) $n = 4$; (*d*) $n = 5$.

3.1.3. *Asymptotic analysis for small forcings* $\varepsilon p \ll 1$

In this section, we solve (3.2)–(3.4) using a multiple scale analysis (e.g. Kevorkian & Cole 1996), assuming that the product $\varepsilon p \ll 1$ remains small. Since the method is now rather classical (e.g. Le Dizès 2000; Herreman *et al.* 2009; Cébron *et al.* 2012*b*), we only give a short outline of the calculation. One first finds the trajectory as

$$\boldsymbol{X}(t) = \boldsymbol{X}^{(0)}(t) + \varepsilon p \boldsymbol{X}^{(1)}(t) + O(\varepsilon^2 p^2). \tag{3.9}$$

Here $\boldsymbol{X}^{(0)}(t)$ is the circular trajectory induced by the solid-body rotation and $\boldsymbol{X}^{(1)}(t)$ deviations induced by the multipolar deformation (see § A.1 for the expressions of $\boldsymbol{X}^{(0)}(t)$ and $\boldsymbol{X}^{(1)}(t)$). With this, one can evaluate ∇U on the perturbed trajectory, up to order $O(\varepsilon p)$, allowing one to solve for the wavenumber:

$$\boldsymbol{\mathcal{K}}(t) = \boldsymbol{\mathcal{K}}^{(0)}(t) + \varepsilon p \boldsymbol{\mathcal{K}}^{(1)}(t) + O(\varepsilon^2 p^2). \tag{3.10}$$

At lowest order, we get

$$\boldsymbol{\mathcal{K}}^{(0)}(t) = \mathcal{K}_0[\sin(\xi)\cos(t + \phi)\boldsymbol{e}_x + \sin(\xi)\sin(t + \phi)\boldsymbol{e}_y + \cos(\xi)\boldsymbol{e}_z]. \tag{3.11}$$

Each wavenumber is specified by a magnitude $\mathcal{K}_0$, angle ξ and initial phase ϕ. This rotating wavenumber is actually stationary in the rotating frame and represents a plane wave there. The first-order deviation $\boldsymbol{\mathcal{K}}^{(1)}(t)$ is important in the stability calculation

and its expression is thus given in §A.1. At leading order, for $\varepsilon p = 0$, these equations can be reduced to a harmonic equation for the amplitude a_z of the axial velocity plane-wave perturbation,

$$\frac{\mathrm{d}^2 a_z^{(0)}}{\mathrm{d}t^2} + \Lambda^2 a_z^{(0)} = 0, \tag{3.12}$$

showing that the amplitude oscillates with angular frequency $\Lambda = \pm 2\cos\xi$. This can be identified as the usual inertial wave dispersion relation in an unbounded fluid domain. We modify the expansion to make a superposition of two waves

$$a_z = [c_1 \, \mathrm{e}^{\mathrm{i}\Lambda t} + c_2 \, \mathrm{e}^{-\mathrm{i}\Lambda t} + \varepsilon p a_z^{(1)}] \, \mathrm{e}^{\varepsilon p \hat{\sigma} t} \tag{3.13}$$

and give them a common but small growth rate $\sigma = \varepsilon p \hat{\sigma}$ ($\hat{\sigma}$ being our unknown). Injecting this into the $O(\varepsilon p)$ balance, we get an equation of the form

$$\frac{\mathrm{d}^2 a_z^{(1)}}{\mathrm{d}t^2} + \Lambda^2 a_z^{(1)} = \sum_{j \in \mathbb{Z}} [F_j \, \mathrm{e}^{\mathrm{i}(\Lambda + j\omega)t} + G_j \, \mathrm{e}^{\mathrm{i}(-\Lambda + j\omega)t}]. \tag{3.14}$$

Secular terms on the right-hand side appear for all resonant frequencies

$$\Lambda_j = \pm j\omega/2, \quad j \leqslant j_{max}, \tag{3.15}$$

with $j \in \mathbb{N}^*$ and $0 < 4/\omega - j_{max} \leqslant 1$. Owing to the inertial wave dispersion relation, each value of j corresponds to a resonant angle $\xi_j = \arccos(j\omega/4)$. These resonant angles, found in the limit $\varepsilon p \ll 1$, are the points where the Floquet resonance tongues emanate. Note that $j_{max} = 1$ for $\omega > 2$, which means that only one Floquet tongue exists (see figure 3). The bounds for j_{max} also show that no instability is possible for $|\omega| > 4 + O(\varepsilon p)$. This is called the forbidden zone of the LDMI (see e.g. Le Bars *et al.* (2007), for the forbidden zone of the TDEI). Note that, at order one in εp, this band is extended to $|\omega| > 4 + \varepsilon p + O(\varepsilon^2 p^2)$ (exactly as for the case considered by Le Dizès (2000)). The growth rate σ is found after posing the solvability condition: multiply the right-hand side by $\exp(\pm \mathrm{i}\Lambda_j t)$ and integrate over a period $2\pi/\Lambda_j$. We then find a homogeneous system of algebraic equations for c_1 and c_2, which defines the growth rate (valid for $\omega \neq 0$):

$$\sigma^* = \frac{\sigma}{\varepsilon p (n-1)|2C|^{n/2-1}} = \frac{16 + (j\omega)^2}{64} |J_{j-1}(n\Delta\varphi) + J_{j+1}(n\Delta\varphi)|. \tag{3.16}$$

The coefficient C relates to the streamline (and thus initial position) under consideration. The maximum growth rate is obtained on the most deformed boundary streamline where $C = -1/2$. We recognize the Bessel function factor (equal to $4f_j$) of (2.17), which shows that each frequency component in the basic flow can couple different pairs of resonant modes, a particular feature of the LDMI.

Figure 4 shows that the analytical asymptotic growth rate given by (3.16) allows a quite accurate prediction of the growth rate for values of β_n up to 0.3. As expected, the results differ for large β_n but in a rather small extent. In figure 4, the libration frequency is greater than 2 ($\omega = 3$), and only one resonance is thus possible ($j_{max} = 1$). In most cases, several resonances are possible, and figure 5(*a*) compares the formula (3.16) with the exact solution of the stability equation in such a case ($\omega = 1 \Rightarrow j_{max} = 3$), showing that the ε dependence is exactly captured. Note that, for a given ω, the local growth rate can go to zero for particular values of ε. Again, this is a particular feature of the LMDI. When the libration angle $\Delta\varphi = \varepsilon/\omega$ is
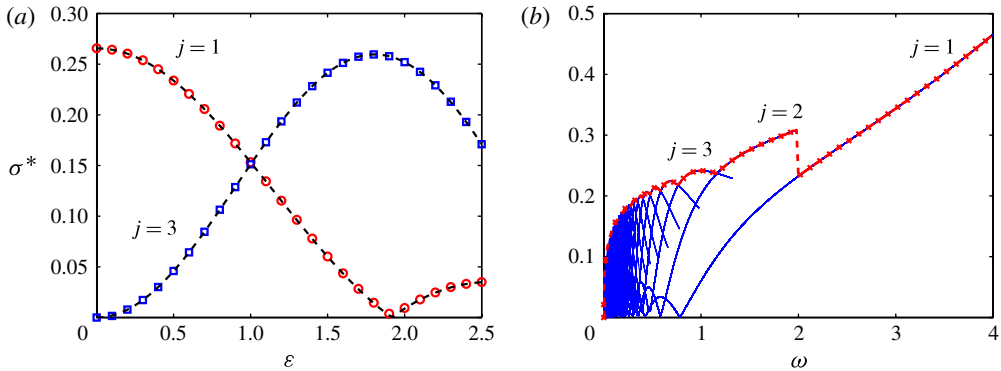
FIGURE 5. (Colour online) (a) Reduced growth rate σ^* against the libration amplitude ε for the two resonances $j = 1$ and $j = 3$ ($n = 2$, $\omega = 1$) in the limit of small deformation p. Symbols (circles (red online) for $j = 1$; squares (blue online) for $j = 3$) are obtained by a direct numerical solution of the stability equations (3.2)–(3.4) with $p = 0.015$, whereas the dashed lines correspond to the analytical formula (3.16), obtained for $\varepsilon p \ll 1$. (b) Plot of σ^* against the libration frequency ω ($n = 3$, $\varepsilon = 1$), for all the resonances $j \in 1, \ldots, j_{max}$ (solid lines; blue online). The number of resonances j_{max} changes with ω. The envelope gives the maximum growth rate σ^* for a given ω (dashed line with cross symbols; red online).

Parameter	Definition
$\boldsymbol{a}$	Amplitude of the velocity plane-wave perturbation
$\mathcal{K}$	Local wavevector along a Lagrangian trajectory
ξ	Initial angle of $\mathcal{K}$ with the vorticity axis $\boldsymbol{e}_z$
T	Turnover period along a pathline
p	Multipolar deformation amplitude
ϖ_i	Floquet exponents of the monodromy matrix $\boldsymbol{a}(T)$
$\Lambda = \pm 2 \cos \xi$	Angular frequency of the inertial wave in an unbounded domain
j	Difference (in ω units) between the angular frequencies of the resonant inertial waves
$\hat{\cdot} = \cdot/(\varepsilon p)$	Operator (dividing the quantity by εp)
σ	Inviscid growth rate
σ^*	Scaled maximum inviscid growth rate (defined by (3.8))
σ_v	Viscous growth rate
k, m, l	Radial, azimuthal and axial wavenumbers of the inertial waves in a bounded geometry
λ	Angular frequency of the inertial wave in a bounded domain
ς	Frequency detuning
α_w	Viscous damping of the resonant inertial waves ($w = 1, 2$)

TABLE 3. Stability analysis parameters.

such that $\mathrm{J}_{j-1}(n\Delta\varphi) + \mathrm{J}_{j+1}(n\Delta\varphi) = 0$, the base flow does not have $j\omega$ frequency content (see (2.17)) and instability is then impossible. Figure 5(b) completes this description of multiple resonances by representing the results of (3.16) as a function of ω. This clearly shows the decrease in the number of resonances when ω is increased.

We now consider two different interesting limit cases of the formula (3.16): the case of large libration forcing $\varepsilon \gg \omega/n$, and then the case of small libration forcing $\varepsilon \ll \omega/n$. Note that the formula (3.16) has been obtained in the limit of small

forcing $\varepsilon p \ll 1$ (p or ε can thus have finite values if the other one is very small). This imposes that the limit $\varepsilon \gg \omega/n$ is actually $\omega p/n \ll \varepsilon p \ll 1$ whereas the other one is given by $\varepsilon p \ll \min(1, \omega p/n)$.

First, we focus on the scaling of σ^* when $\omega p/n \ll \varepsilon p \ll 1$, which implies $n\Delta\varphi \gg 1$. This limit case is interesting because it allows us to test the possibility of an LDMI excited by a small-scale periodic pattern in the boundary roughness ($n \gg 1$). In this case, using $J_{j-1}(x) + J_{j-1}(x) = 2j J_j(x)/x$, we obtain

$$\sigma^* = \frac{16 + (j\omega)^2}{32} j \sqrt{\frac{2}{\pi(n\Delta\varphi)^3}} \, |\cos(n\Delta\varphi - j\pi/2 - \pi/4)| + O\left(\frac{1}{(n\Delta\varphi)^{5/2}}\right). \quad (3.17)$$

Then, the maximum growth rate is reached for $j = j_{max} \approx 4/\omega$ and reads

$$\sigma^* \sim 4\sqrt{\frac{2\,\omega}{\pi n^3\,\varepsilon^3}} \quad \Rightarrow \quad \sigma \sim 4p\,|2C|^{n/2-1}\sqrt{\frac{2\,\omega}{\pi n\varepsilon}}. \quad (3.18)$$

The growth rate σ thus decreases towards 0 as $n^{-1/2}$ in the limit $n \gg \omega/\varepsilon$. Considering a boundary of arbitrary shape with many multipolar components ($n = 2, 3, \ldots$), this shows that the instabilities excited by the lowest orders n will be the more unstable.

The opposite limit case $n\Delta\varphi \ll 1$ corresponds to the asymptotic regime of small libration forcings $\varepsilon \ll \omega/n$, which is the relevant limit in geophysics. In this case, only the first resonance $j = 1$ can contribute (since $J_0(0) = 1$ and for all $j \neq 0$, $J_j(0) = 0$). We then have a single unstable mode with rescaled growth rate

$$\sigma^* = \frac{16 + \omega^2}{64}, \quad (3.19)$$

which is in agreement with the result previously obtained in the particular case $n = 2$ (Cébron *et al.* 2012*a,c*). In the limit of $\omega \to 0$ (absence of libration), i.e. in the limit of the so-called synchronization state in an astrophysical context (e.g. Cébron *et al.* 2012*b*), the growth rate tends towards $\sigma^* = 1/4$. This limit can also be obtained from the results of Le Dizès (2000), who considers the case of a constant non-zero differential rotation between the multipolar strain and the fluid. In the limit of infinitesimal multipolar deformation, this case leads to an instability only for $n \leqslant 4$, and Le Dizès (2000) shows that the maximum inviscid growth rate is then given by (using the constant differential rotation as the time scale)

$$\frac{\bar{\sigma}}{p} = \frac{[n + 4(1 + \Omega^G)]^2}{64(1 + \Omega^G)^2}(n - 1), \quad (3.20)$$

where $\Omega^G = \Omega_{orb}/(\Omega - \Omega_{orb})$, with Ω_{orb} the rotation rate of the strain in the inertial frame. The expression (3.20) is consistent with the expression (3.19) in the limit of a synchronized state: $\Omega_{orb}/\Omega_{spin} = 1 - \varepsilon$, i.e. $|1 + \Omega^G| \sim |\Omega^G| = 1/\varepsilon$ and $\bar{\sigma} = \sigma/\varepsilon$ (to have the same time scale).

3.2. *Global stability analysis*

3.2.1. *Problem definition*

The linear stability problem for the perturbation flow $\boldsymbol{u}$ and modified pressure π can be written as

$$\partial_t \boldsymbol{u} + \boldsymbol{U} \cdot \nabla \boldsymbol{u} + \boldsymbol{u} \cdot \nabla \boldsymbol{U} + 2\boldsymbol{e}_z \times \boldsymbol{u} = -\nabla\pi + E\,\Delta\boldsymbol{u}, \quad \nabla \cdot \boldsymbol{u} = 0, \quad (3.21)$$

in the rotating frame of reference (R) used for our global analysis. We will again omit the use of these superscripts. No-slip boundary conditions are imposed on the

deformed cylinder's surface. We adopt a four-vector notation $\boldsymbol{Y} = [u_r, u_\theta, u_z, \pi]^{\mathrm{T}}$, so that the problem may be rewritten in compact form as

$$\mathscr{L}\boldsymbol{Y} = \varepsilon p[\mathrm{e}^{\mathrm{i}n\theta}f(t)\mathscr{N} + \mathrm{c.c.}]\boldsymbol{Y} + E\mathscr{V}\boldsymbol{Y}. \tag{3.22}$$

The operators $\mathscr{L}$, $\mathscr{N}$ and $\mathscr{V}$ are defined in § A.2.1. We can now investigate the stability of the flow using an asymptotic model, valid for small forcings $\varepsilon p \ll 1$ and small Ekman numbers $E \ll 1$.

3.2.2. *Leading-order solution: inertial waves in cylinders*

In the absence of boundary deformation $(p = 0)$ and viscosity $(E = 0)$, the perturbation flow is the solution of

$$\mathscr{L}\boldsymbol{Y}^{(0)} = 0, \quad u_r^{(0)}(1, \theta, z, t) = 0. \tag{3.23}$$

The solution to this problem is a general superposition of inertial waves in cylindrical geometry:

$$\boldsymbol{Y}^{(0)}(r, \theta, z, t) = \sum_{ml\lambda} A_{ml\lambda}\boldsymbol{Q}_{ml\lambda}(r)\,\mathrm{e}^{\mathrm{i}m\theta}\,\mathrm{e}^{\mathrm{i}lz}\,\mathrm{e}^{\mathrm{i}\lambda t}. \tag{3.24}$$

Here $A_{ml\lambda}$ are arbitrary amplitudes. Each wave is specified by an angular frequency $\lambda \in [-2, 2]$, an azimuthal wavenumber $m \in \mathbb{Z}$ and an axial wavenumber $l = 2\pi n_z/h$, with $n_z \in \mathbb{Z}$ the number of axial wavelengths. Note that both λ and Λ denote inertial wave frequencies, but the former is related to inertial waves in a radially bounded cylinder, whereas the latter is related to those in an unbounded medium. The radial profiles $\boldsymbol{Q}_{ml\lambda}$ are solutions of $\mathscr{L}_{ml\lambda}\boldsymbol{Q}_{ml\lambda} = 0$, where $\mathscr{L}_{ml\lambda}$ corresponds to the operator $\mathscr{L}$ in which replacements $\partial_t \to \mathrm{i}\lambda$, $\partial_\theta \to \mathrm{i}m$ and $\partial_z \to \mathrm{i}l$ have been made. We find

$$\boldsymbol{Q}_{ml\lambda} = \begin{bmatrix} [(2-\lambda)\,\mathrm{J}_{m+1}(kr) + (2+\lambda)\,\mathrm{J}_{m-1}(kr)]\,/2 \\ -\mathrm{i}\,[(2-\lambda)\,\mathrm{J}_{m+1}(kr) - (2+\lambda)\,\mathrm{J}_{m-1}(kr)]\,/2 \\ -\mathrm{i}(k\lambda/l)\,\mathrm{J}_m(kr) \\ \mathrm{i}(k\lambda^2/l^2)\,\mathrm{J}_m(kr) \end{bmatrix}, \quad k^2 = \frac{(4-\lambda^2)}{\lambda^2}\,l^2. \tag{3.25}$$

The radial wavenumber k and the frequencies are discretized by the boundary conditions on the surface $r = 1$, which, together with the previous definition of k, fixes the inertial wave dispersion relation:

$$(2-\lambda)\,\mathrm{J}_{m+1}(k) + (2+\lambda)\,\mathrm{J}_{m-1}(k) = 0, \quad \lambda = \pm 2\sqrt{\frac{l^2}{k^2 + l^2}}. \tag{3.26}$$

For fixed m, l and both possible signs of the frequency, this equation admits a countable infinite number of discrete radial wavenumbers, which are easily identified numerically. We label these radial wavenumbers of the frequency with a radial counter $n_r = 1, 2, \ldots$. A wave is entirely determined by the set (k, m, l, λ) or alternatively (n_r, m, n_z, λ) in a cylinder with fixed height. The frequency λ is such that $\lambda \in [-2, 2]$, which is a general property of inertial waves.

3.2.3. *Inviscid growth rate σ at resonance*

As in the local theory, we will now propose an asymptotic solution that is a superposition of two waves and a remainder:

$$\boldsymbol{Y} = (c_1\boldsymbol{Q}_1(r)\,\mathrm{e}^{\mathrm{i}m_1\theta}\,\mathrm{e}^{\mathrm{i}\lambda_1 t} + c_2\boldsymbol{Q}_2(r)\,\mathrm{e}^{\mathrm{i}m_2\theta}\,\mathrm{e}^{\mathrm{i}\lambda_2 t} + \varepsilon p\boldsymbol{Y}^{(1)})\,\mathrm{e}^{\mathrm{i}lz}\,\mathrm{e}^{\varepsilon p\hat{\sigma}t} + O(\varepsilon p^2). \tag{3.27}$$

Here $\boldsymbol{Q}_j$ is shorthand for $\boldsymbol{Q}_{m_j l_j \lambda_j}$. We search for an expression for the growth rate $\sigma = \varepsilon p \hat{\sigma}$. Injecting this ansatz into the previous system of (3.22) we have

$$\mathscr{L} \boldsymbol{Y}^{(1)} = [-\hat{\sigma} \, \mathscr{J} + (\mathrm{e}^{\mathrm{i}n\theta} f(t) \mathscr{N} + \mathrm{c.c.})]$$
$$\times [c_1 \boldsymbol{Q}_1(r) \, \mathrm{e}^{\mathrm{i}m_1\theta} \, \mathrm{e}^{\mathrm{i}\lambda_1 t} + c_2 \boldsymbol{Q}_2(r) \, \mathrm{e}^{\mathrm{i}m_2\theta} \, \mathrm{e}^{\mathrm{i}\lambda_2 t}]. \tag{3.28}$$

The right-hand side is secularly forcing the left-hand side, whenever two waves satisfy resonance conditions

$$m_1 + n = m_2, \quad l_1 = l_2 = l, \quad \lambda_1 + j\omega = \lambda_2, \tag{3.29}$$

for $j \in \mathbb{Z}$. This is the global equivalent of (3.15). Considering the inertial wave dispersion relation, this is a quite restrictive constraint that certainly not all pairs of inertial waves will be able to satisfy. Exact resonances cannot be found when $|j\omega| > 4$ because $\lambda_1, \lambda_2 \in [-2, 2]$. We denote each resonance in shorthand form by a quintuplet (m_1, m_2, n_r, n_z, j). Here n_r is the radial wavenumber label and n_z is the number of vertical wavelengths. As in the study of Eloy, we systematically find the largest growth rates for central couplings that pair waves with the same radial label $n_{r,1} = n_{r,2}$, synonymous for $k_1 \simeq k_2$. The field $\boldsymbol{Y}^{(1)}$ is necessarily composed of

$$\boldsymbol{Y}^{(1)} = \boldsymbol{Z}_1(r, z) \, \mathrm{e}^{\mathrm{i}m_1\theta} \, \mathrm{e}^{\mathrm{i}\lambda_1 t} + \boldsymbol{Z}_2(r, z) \, \mathrm{e}^{\mathrm{i}m_2\theta} \, \mathrm{e}^{\mathrm{i}\lambda_2 t} + \boldsymbol{Z}_{NR}(r, \theta, z, t). \tag{3.30}$$

The last term $\boldsymbol{Z}_{NR}$ absorbs non-resonant contributions. Inserted into the previous equation, we get the secularly forced system:

$$\mathscr{L}_1 \boldsymbol{Z}_1 = -\hat{\sigma} c_1 \mathscr{J} \boldsymbol{Q}_1 + f_j c_2 \mathscr{N}^\dagger \boldsymbol{Q}_2, \tag{3.31}$$

$$\mathscr{L}_2 \boldsymbol{Z}_2 = -\hat{\sigma} c_2 \mathscr{J} \boldsymbol{Q}_2 + f_j c_1 \mathscr{N} \boldsymbol{Q}_1. \tag{3.32}$$

Here $\mathscr{L}_i = \mathscr{L}_{m_i l_i \lambda_i}$. We used $(f^\dagger)_{-j} = f_j$ in (3.31) (see (2.17)). A solvability condition fixes the growth rates, but in order to write it, we need a well-adapted scalar product. We choose here

$$\langle \boldsymbol{Q}_1, \boldsymbol{Q}_2 \rangle = \int_0^1 \left(\sum_{\mu=1}^4 Q_{1,\mu}^\dagger Q_{2,\mu} \right) r \, \mathrm{d}r. \tag{3.33}$$

This scalar product is advantageous for our calculations, because direct and adjoint inertial modes are then identical (Eloy *et al.* 2003). Indeed, if we consider that adjoint modes satisfy the same boundary conditions as direct modes (a zero normal velocity), an integration by parts gives (noting the adjoint with a superscript A)

$$\langle \boldsymbol{Q}_{ml\lambda}^A, \mathscr{L}_{ml\lambda} \boldsymbol{Q}_{ml\lambda} \rangle = -\langle \mathscr{L}_{ml\lambda} \boldsymbol{Q}_{ml\lambda}^A, \boldsymbol{Q}_{ml\lambda} \rangle. \tag{3.34}$$

The adjoint operator is thus the opposite of the direct operator ($\mathscr{L}_{ml\lambda}^A = -\mathscr{L}_{ml\lambda}$), and direct and adjoint modes are identical with this scalar product.

The solvability condition is expressed by projecting (3.31) and (3.32) onto $\boldsymbol{Q}_1$ and $\boldsymbol{Q}_2$. On the left-hand side, we use a partial integration and the definition of the adjoint modes, e.g. for the first equation:

$$\langle \boldsymbol{Q}_1, \mathscr{L}_1 \boldsymbol{Z}_1 \rangle = -\langle \underbrace{\mathscr{L}_1 \boldsymbol{Q}_1}_{0}, \boldsymbol{Z}_1 \rangle + Q_{1,4}^\dagger(1) Z_{1,1}(1). \tag{3.35}$$

This process introduces boundary terms that appeal for first-order corrections $Z_{1,1}$ and $Z_{2,1}$ of the radial velocities of the modes. It is through these terms that $O(p)$ couplings related to boundary deformation (see §A.2.2 for more details) arrive in the global

stability analysis. The solvability condition thus results in a homogenous system of two algebraic equations:

$$c_1(-\sigma \mathscr{J}_{11}) + c_2(\varepsilon p f_j \mathscr{N}_{12} - p g_j \mathscr{B}_{12}) = 0, \tag{3.36}$$

$$c_2(-\sigma \mathscr{J}_{22}) + c_1(\varepsilon p f_j \mathscr{N}_{21} - p g_j \mathscr{B}_{21}) = 0, \tag{3.37}$$

with matrix elements

$$\mathscr{J}_{11} = \langle \boldsymbol{Q}_1, \mathscr{J} \boldsymbol{Q}_1 \rangle, \quad \mathscr{N}_{12} = \langle \boldsymbol{Q}_1, \mathscr{N}^\dagger \boldsymbol{Q}_2 \rangle, \tag{3.38a}$$

$$\mathscr{J}_{22} = \langle \boldsymbol{Q}_2, \mathscr{J} \boldsymbol{Q}_2 \rangle, \quad \mathscr{N}_{21} = \langle \boldsymbol{Q}_2, \mathscr{N} \boldsymbol{Q}_1 \rangle, \tag{3.38b}$$

and boundary terms

$$\mathscr{B}_{12} = Q_{1,4}^\dagger(1) \left(-\frac{1}{n} \partial_r Q_{2,1}(1) - \mathrm{i}\, Q_{2,2}(1) \right), \tag{3.39a}$$

$$\mathscr{B}_{21} = Q_{2,4}^\dagger(1) \left(-\frac{1}{n} \partial_r Q_{1,1}(1) + \mathrm{i}\, Q_{1,2}(1) \right). \tag{3.39b}$$

We used $(g^\dagger)_{-j} = g_j$ in (3.36). Elimination of c_1 and c_2 results in an equation for the inviscid growth rate at resonance:

$$\sigma^2 = \frac{(\varepsilon f_j \mathscr{N}_{12} - g_j \mathscr{B}_{12})(\varepsilon f_j \mathscr{N}_{21} - g_j \mathscr{B}_{21})}{\mathscr{J}_{11} \mathscr{J}_{22}} p^2. \tag{3.40}$$

We have instability only when the real part of the right-hand side is positive. Note that the relation c_1/c_2 is fixed by one of the equations of (3.36).

3.2.4. *Frequency detuning and viscous damping: growth rate σ_v*

Pairs of waves that perfectly satisfy resonance conditions (3.29) can only exist in cylinders with well-chosen height h, or for well-defined frequencies $j\omega$. These conditions may however be relaxed in order to admit imperfect resonance. In the present article, we build in these detuning effects through a frequency detuning. Imperfect resonance then supposes that

$$\lambda_1 + j\omega = \bar{\lambda} + \varsigma, \quad \lambda_2 = \bar{\lambda} - \varsigma, \tag{3.41}$$

with $\varsigma = \varepsilon p \hat{\varsigma} \ll 1$ a small frequency detuning and $\bar{\lambda}$ a modified resonant frequency. This detuning is introduced in the model by modifying the asymptotic ansatz into

$$\boldsymbol{Y} = (c_1 \boldsymbol{Q}_1(r)\, \mathrm{e}^{\mathrm{i}m_1\theta}\, \mathrm{e}^{\mathrm{i}(\bar{\lambda}-j\omega)t} + c_2 \boldsymbol{Q}_2(r)\, \mathrm{e}^{\mathrm{i}m_2\theta}\, \mathrm{e}^{\mathrm{i}\bar{\lambda}t} + \varepsilon p \boldsymbol{Y}^{(1)})\, \mathrm{e}^{\mathrm{i}lz}\, \mathrm{e}^{\varepsilon p \hat{\sigma} t} + O(\varepsilon p^2). \tag{3.42}$$

Starting from this ansatz, the solvability condition leads to the set of equations (3.36) and (3.37) in which $-\sigma \to -\sigma + \mathrm{i}\varsigma$ in (3.36) and $-\sigma \to -\sigma - \mathrm{i}\varsigma$ in (3.37) are modified.

Viscous corrections induced by boundary layers, which scale as $\sqrt{E}$, formally enter the model through boundary terms as (3.39) as boundary-layer pumping modifies the radial velocity at order $\sqrt{E}$. Volume damping can be formally introduced through the operator $\mathscr{V}$. Still, since viscous effects are not modified by the libration at lowest order, it is sufficient to use a pre-existing formula (Kerswell & Barenghi 1995). Waves with positive frequencies $\lambda_j > 0$ have a damping

$$\alpha_w = \sqrt{E}\, \frac{(1+\mathrm{i})}{4\sqrt{2}}\, \frac{(4 - \lambda_w^2)(m_w^2 + l_w^2)\sqrt{\lambda_w}}{(m_w^2 + l_w^2 - m_w \lambda_w/2)} + E(k_w^2 + l_w^2), \tag{3.43}$$

for $w = 1, 2$. If $\lambda_w < 0$ we need to use the complex conjugate formula. Viscosity is introduced in the previous set of equations (3.36) and (3.37) by modifying $-\sigma \to -\sigma - \alpha_w$ in both equations. Combining the effects of both viscous damping and frequency detuning into a growth rate denoted σ_v, we have

$$\tilde{\sigma}_v = -\frac{\alpha_1 + \alpha_2}{2} + \frac{1}{2}\sqrt{(\alpha_1 - \alpha_2)^2 - 2i\varsigma(\alpha_1 - \alpha_2) + 4(\sigma^2 - \varsigma^2)}. \tag{3.44}$$

We have instability when the real part $\sigma_v = \mathrm{Re}(\tilde{\sigma}_v)$ is positive.

3.3. *Parameter survey*

In the practical implementation of global stability, we fix the cylinder height h and vary the libration frequency ω. Then, as described in §3.2.4 (see (3.41)), imperfect resonances are taken into account via a frequency detuning, as in Gledzer & Ponomarev (1992), Kerswell (1993a), Lacaze *et al.* (2004) and Herreman *et al.* (2010). Note that, as in Eloy *et al.* (2003) or Lagrange *et al.* (2011), we can also calculate imperfect resonances by fixing $\lambda_1 + j\omega = \lambda_2$ and relaxing the resonant constraint on the axial wavenumber ($l_1 - l_2 = O(p)$). However, this method is less efficient for large coupling frequencies $j\omega \simeq 4$.

To calculate σ_v, we thus find all the waves,

$$\text{mode 1 } (n_r, m_1, n_z, \lambda_1), \quad \text{mode 2 } (n_r, m_2, n_z, \lambda_2), \tag{3.45}$$

with numbers

$$n_r = 1, \ldots, n_{r,max}, \quad \begin{cases} m_1 = -n + 1, \ldots, m_{1,max}, \\ m_2 = 1, \ldots, m_{1,max} + n, \end{cases} \quad n_z = 1, \ldots, n_{z,max}, \tag{3.46}$$

and both positive and negative frequencies, that solve the dispersion relation (3.26). For each pair of waves, we then know exactly the resonant frequencies

$$\omega = (\lambda_2 - \lambda_1)/j, \quad |j| \in 1, \ldots, j_{max}, \tag{3.47}$$

so that the resonance conditions (3.29) are exactly satisfied. Since $|\lambda_2 - \lambda_1| \leqslant 4$ maximally, modes with $|j| \neq 1$ exist within bands $\omega \in [0, 4/|j|]$. Note also that only central couplings with $n_{r,1} = n_{r,2} = n_r$ are considered here; we tested that they always have significantly larger growth rates (as in Eloy *et al.* (2003)). We take into account (through j) that a given pair of modes may be destabilized by different frequencies. For each of these wave pairs, we also calculate all the necessary matrix elements and damping coefficients. All this information is stored for a post-processing phase in which we can vary ε, $\Delta\varphi$, E and p and consider the effect of detuning ς. (Practical information on the implementation of the global instability analysis can be found in a series of commented MATLAB scripts that are available online as supplementary material at http://dx.doi.org/10.1017/jfm.2013.623.) Here we discuss some particular features of the global stability theory. Further, we will perform a systematic comparison with numerical results.

3.3.1. *Inviscid growth rate σ versus ω*

The non-viscous stability of a given pair of modes entirely depends on the sign of the two frequencies λ_1 and λ_2. We observe that when the frequencies of the waves have the same sign, $\mathrm{Sgn}(\lambda_1\lambda_2) = +1$, then the inviscid growth rate σ is purely imaginary, so that these pairs of modes can never be destabilized (with Sgn the sign function). If, on the contrary, frequencies have an opposite sign, $\mathrm{Sgn}(\lambda_1\lambda_2) = -1$, we always have a real σ and so inviscid instability. With the convention that $\omega > 0$,
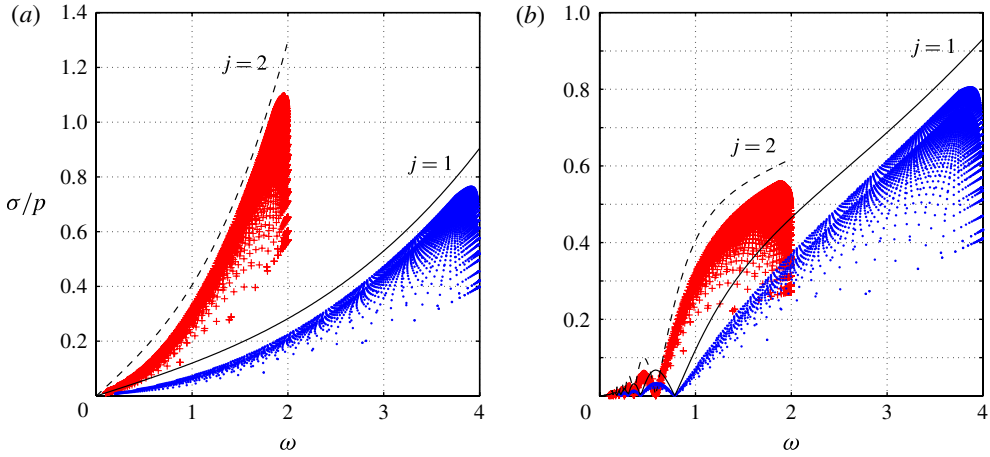
FIGURE 6. (Colour online) Rescaled inviscid growth rates σ/p at resonance as a function of ω, for different values of $j = 1, 2$ as marked in the figure and comparison with maximum local instability growth rate ((3.16) with $C = -1/2$) (full and dashed lines). We consider triangular deformation $n = 3$ in a cylinder with height $h = 2$. (*a*) Here we fix the libration angle $\Delta\varphi = 1$; (*b*) we fix the libration amplitude $\varepsilon = 1$. The survey involves all modes up to $n_{r,max} = 2$, $m_{1,max} = 50$, $n_{z,max} = 50$.

we have also noticed that modes with $\lambda_1 < 0$ and $\lambda_2 > 0$ and thus $j > 0$ are always much more unstable than the opposite case. We therefore concentrate on this type of mode. We finally observe that the couplings with the lowest radial labels, $n_r = 1$, but the highest azimuthal wavenumbers, m_1, and the largest number of axial wavelengths, n_z, are generally the most unstable in the inviscid limit. This explains why we used $n_{r,max} = 2$, $m_{1,max} = 50$, $n_{z,max} = 50$ for this inviscid study.

In figure 6, we show inviscid growth rates at resonance for a triangular ($n = 3$) deformation, at fixed libration angle $\Delta\varphi = 1$ (figure 6a) and for fixed libration amplitude $\varepsilon = 1$ (figure 6b). Each point represents a different unstable pair of modes at resonance. We only show two different $j = 1, 2$ so as not to overload the figures. It is particularly important to notice that couplings with $j = 2$ may become more unstable than couplings with $j = 1$ in the interval $\omega \in [0, 2]$, a consequence of the large frequency content of the libration-driven basic flow at large ε or large libration angles $\Delta\varphi$. In the numerical simulations, ε is always large, so it is important to take this effect into account.

The local instability analysis estimate (full and dashed lines) provide excellent upper bounds over the entire ω span and for both $j = 1, 2$. Note also in figure 6(*b*) how the local growth rate of a given resonance may drop to zero for particular frequencies at fixed j as a consequence of the Bessel function correction (see (3.16)). This feature is well reproduced in the global growth rates.

3.3.2. *Corrected growth rate σ_v versus ω*

The inviscid growth rates at resonance do not give a very realistic picture, as modes with high wavenumbers can be strongly damped by viscosity. In figure 7(*a*), we show the maximal viscous growth rate $\max(\sigma_v)$ as a function of ω for $\varepsilon = 1$, $p = 0.2$, $h = 2$ and different E numbers (data from survey $n_{r,max} = m_{1,max} = n_{z,max} = 10$, $j_{max} = 4$). At low E, we see that the maximal growth rate follows a bumpy curve that has a shape that is quite close to the envelope of figure 6(*b*). Above $\omega > 2$, only $j = 1$ couplings
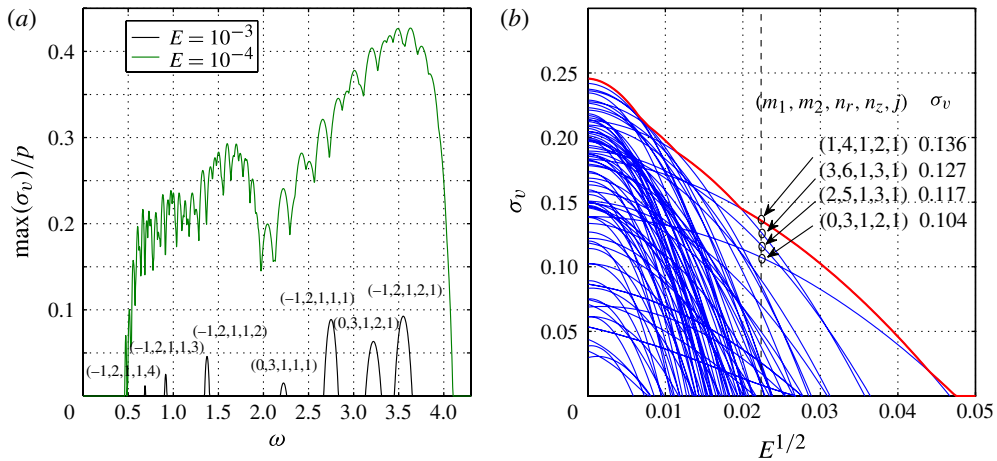
FIGURE 7. (Colour online) LDMI growth rates in triangularly deformed cylinder ($n = 3$) for $h = 2$ and $\varepsilon = 1$. (*a*) Maximal viscous growth rates $\max(\sigma_v)/p$ as a function of ω for $E = 10^{-3}$ and 10^{-4} and $p = 0.2$. For $E = 10^{-3}$, we identify unstable couplings (m_1, m_2, n_r, n_z, j). (*b*) Growth rate σ_v as a function of $E^{1/2}$ for $h = 2$ and $p = 0.45$. We identify the four most unstable couplings and give the numerical values for σ_v at $E = 5 \times 10^{-4}$ (parameters studied numerically in § 4). The thicker line (red online) is the envelope of the resonance curves.

survive. The instability domain is slightly extended in the forbidden zone $\omega > 4$. Close to threshold, here for $E = 10^{-3}$, we can clearly identify different resonances. In the figure, we added (m_1, m_2, n_r, n_z, j) to characterize the coupling. We see that $n_r = 1$ for all modes, so the radial structures are large. Most resonant peaks combine $(m_1, m_2) = (-1, 2)$, modes with one or two axial wavelengths (n_z) and for $j = 1, 2, 3, 4$. We also see two peaks involving modes $(m_1, m_2) = (0, 3)$ with one or two axial wavelengths.

3.3.3. *Growth rate σ_v versus E*

In figure 7(*b*), each line follows the growth rates of different couplings with respect to $\sqrt{E}$, for fixed $\omega = 3$, $\varepsilon = 1$, $p = 0.45$ and for $h = 2$. The parabolic form of each of these curves is indicative of dominant volume damping for the range of E considered here. However, note that, in the limit of very small E, we naturally expect the boundary dissipation to be dominant (for $E \ll 1$, we have $E^{1/2} \gg E$). Note that the situation is very different in a spherical or even a spheroidal container, where the volume damping exactly vanishes for any inertial mode (Zhang, Liao & Earnshaw 2004) and thus where the viscous damping can only be due to surface effects (e.g. Lacaze *et al.* 2004).

We further identify the four most unstable couplings at $E = 5 \times 10^{-4}$, a configuration that will be studied numerically, and mark (m_1, m_2, n_r, n_z, j) in the figure, together with the numerical value of the growth rate σ_v. Modes with higher azimuthal wavenumbers $(m_1, m_2) = (1, 4), (3, 6), (2, 5), (0, 3)$ dominate and we count $n_z = 2, 3$ axial wavelengths.

4. Numerical simulations of libration-driven multipolar flow

In this section, we present simulations of libration-driven multipolar flows. First, we provide some details on the computational method (§ 4.1). Then, in § 4.2 we validate

that the basic flow (2.8) is indeed established for two different very simple and experimentally realizable forcings. In the last subsection, we demonstrate the existence of the LDMI, and characterize its properties, such as the growth rate, saturation amplitude and viscous dissipation rate.

4.1. *Numerical method*

To perform our numerical simulations, we use a parallel unstructured finite-volume code (Vantieghem 2011). It is based on a collocated arrangement of the variables, and a second-order centred finite-difference-like discretization stencil for the spatial differential operators. The time advancement algorithm is based on a canonical fractional-step method (Kim & Moin 1985). More specifically, the procedure to obtain the velocity and reduced pressure $\boldsymbol{u}^{N+1}$ and Π^{N+1} at time step $t^{N+1} = t^N + \Delta t$, given the respective variables at time step N, is as follows.

(*a*) We first solve the intermediate velocity $\boldsymbol{u}^\star$ from the equation

$$\frac{\boldsymbol{u}^\star - \boldsymbol{u}^N}{\Delta t} = -\boldsymbol{u}_{AB}^{N+1/2} \cdot \nabla \boldsymbol{u}_{CN}^{N+1/2} - \nabla \Pi^N$$

$$- 2\gamma^{N+1/2}\boldsymbol{e}_z \times \boldsymbol{u}^{N+1/2} + E\nabla^2\boldsymbol{u}_{CN}^{N+1/2} - \frac{\mathrm{d}(\gamma^{N+1/2})}{\mathrm{d}t}\boldsymbol{e}_z \times \boldsymbol{x}, \qquad (4.1)$$

with no-slip boundary condition $\boldsymbol{u}_{bnd}^\star = \boldsymbol{0}$. In this expression, $\boldsymbol{u}_{AB}^{N+1/2}$ and $\boldsymbol{u}_{CN}^{N+1/2}$ denote the velocity at time step $N + 1/2$ obtained using a second-order Adams–Bashforth, respectively Crank–Nicolson approach, i.e.

$$\boldsymbol{u}_{AB}^{N+1/2} = \tfrac{3}{2}\boldsymbol{u}^N - \tfrac{1}{2}\boldsymbol{u}^{N-1}, \qquad (4.2)$$

$$\boldsymbol{u}_{CN}^{N+1/2} = \tfrac{1}{2}(\boldsymbol{u}^N + \boldsymbol{u}^\star). \qquad (4.3)$$

The mixed Adams–Bashforth/Crank–Nicolson formulation for the advective term has the advantage of being kinetic-energy-conserving and time-stable for any Δt (Ham, Mattsson & Iaccarino 2006), and it does not require the solution of a nonlinear system for the unknown $\boldsymbol{u}^\star$.

(*b*) The new velocity $\boldsymbol{u}^{N+1}$ is then related to $\boldsymbol{u}^\star$ by

$$\boldsymbol{u}^{N+1} = \boldsymbol{u}^\star - \Delta t(\Delta \Pi^{N+1}), \qquad (4.4)$$

with $\Delta \Pi^{N+1} = \Pi^{N+1} - \Pi^N$. Imposing the incompressibility constraint on $\boldsymbol{u}^{N+1}$ leads to a Poisson equation for $\Delta \Pi^{N+1}$,

$$\nabla^2(\Delta \Pi^{N+1}) = (\Delta t)^{-1}\nabla \cdot \boldsymbol{u}^\star, \qquad (4.5)$$

with boundary condition $\boldsymbol{e}_n \cdot \nabla(\Delta \Pi^{N+1}) = 0$. This Poisson equation is solved with the algebraic multigrid method BoomerAMG (Henson & Meier Yang 2000).

To discretize the equations in space, we use a grid that is shaped such that its boundary coincides with a streamline of the flow (2.8). To this end, we transform a circular mesh into one bounded by a streamline (see figure 8). This requires an explicit parametrization of the streamlines $r = F(\theta)$, which is derived in appendix B. As shown in figure 8(*a*), we start from a grid whose nodes occur on curves of constant θ or constant r, except for a smaller inner core of radius $r < 0.15$. The outer part of the grid (i.e. for $0.15 \leqslant r \leqslant 1$) consists of highly regular regions of quadrilateral elements, separated by transition layers of triangular elements; these transition layers allow one to decrease the number of grid points in azimuthal direction as $r \to 0$, so

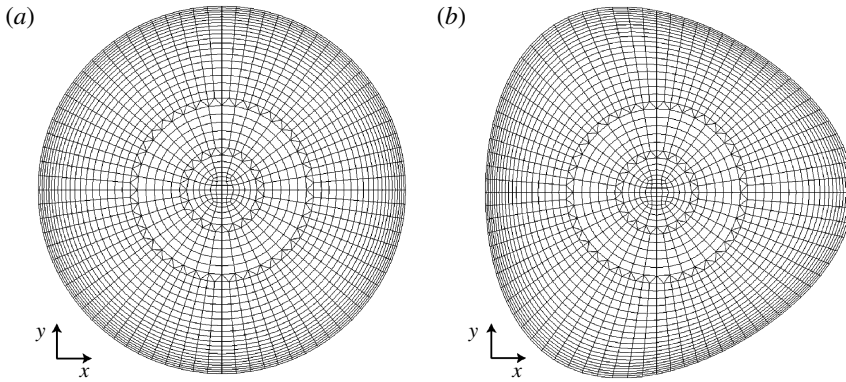FIGURE 8. Illustration of the deformed numerical grid in the *x–y* plane for $p = 0.2$. For clarity, the closer spacing in the boundary-layer region has been left out. (*a*) Initial circular grid before tripolar deformation. (*b*) Final grid after tripolar deformation (4.6)–(4.7).

as to avoid any clustering of the grid points near the origin. The grid consists of quadrilateral elements and is unstructured for $r < 0.15$. Furthermore, the grid points are more closely spaced in the wall-normal direction in the vicinity of $r = 1$ in order to account for the presence of thin viscous boundary layers of thickness $\delta = \sqrt{2E/\omega}$ (Wang 1970); more precisely, the grid spacing in the near-wall region is such that there are at least five grid nodes within a distance δ from the wall. Then, we gradually deform the outer quadrilateral elements, starting at $r_0 = 0.5$ towards $r = 1$. The radial coordinate of the grid nodes is transformed from r into r' according to the following formulae:

$$r' = r \quad \text{for } r \leqslant r_0, \tag{4.6}$$

$$r' = \left[1 + (F(\theta) - 1) \frac{r - r_0}{1 - r_0} \right] r \quad \text{for } r_0 < r \leqslant 1. \tag{4.7}$$

This results in a smooth transformation, in which the grid elements are not too distorted, as shown in figure 8(*b*) for $p = 0.2$. Moreover, we also wish to avoid grid distortion at interfaces between zones of triangular and quadrilateral elements because these interfaces are more sensitive to numerical stability and accuracy problems. Therefore, we choose the value $r_0 = 0.5$ such that the grid deformation only affects the elements in the outer shell of quadrilateral elements. To determine the required grid resolution for the simulations of the LDMI 3D flows, we have first performed a grid convergence study. More specifically, for a given set of typical parameters ($E = 5 \times 10^{-4}$, $n = 3$, $p = 0.45$, $\varepsilon = 1$, $\omega = 3$), we have investigated the dependence of the growth rate σ_v on the number of control volumes N_{CV}. We characterize the spatial resolution using the resolution number R_{grid}, defined by $R_{grid} = N_{CV}^{1/3}$. To estimate the growth rate σ_v, we use the procedure outlined in § 4.3. Our results are summarized in figure 9, where we show the relative difference $\Delta\sigma_v$ between σ_v for a given value of R_{grid} and σ_v for the largest value of R_{grid} that we have considered ($R_{grid} = 167$):

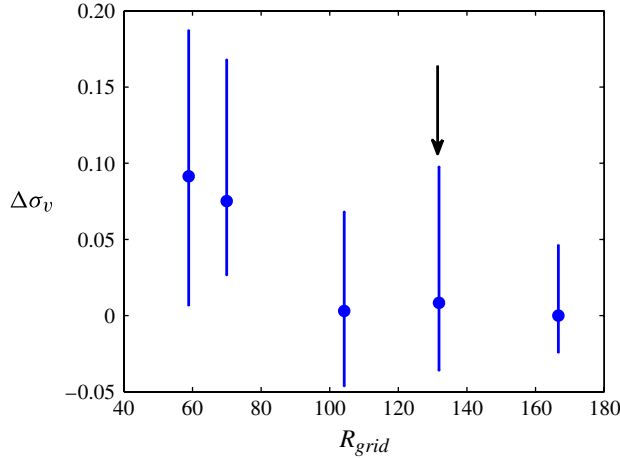$$\Delta\sigma_v = \frac{\sigma_v(R_{grid}) - \sigma_v(R_{grid} = 167)}{\sigma_v(R_{grid} = 167)}. \tag{4.8}$$

FIGURE 9. (Colour online) Convergence of the growth rate of a 3D multipolar instability with increasing grid resolution (for $E = 5 \times 10^{-4}$, $n = 3$, $p = 0.45$, $\varepsilon = 1$, $\omega = 3$). For each simulation at a given mesh resolution R_{grid}, we perform several measures of σ, which gives several measures of the relative difference $\Delta \sigma_v$. We report in this figure the mean value of $\Delta \sigma_v$ (dots), as well as the obtained extremum values (error bars). The arrow indicates the minimal resolution used for the systematic study of the instability in § 4.3.

Figure 9 shows that the relative difference of σ_v is smaller than 0.5 % for $R_{grid} \gtrsim 105$, and much smaller than the uncertainties (error bars) associated with the measure of σ_v. For the systematic study of the multipolar instability discussed below, we systematically work at $R_{grid} \approx 131.8$ (indicated by an arrow in figure 9) for $E \geqslant 5 \times 10^{-4}$, which corresponds to approximately 2.2 million control volumes. For lower Ekman number, we employ grids with up to 2.9 million control volumes (i.e. $R_{grid} \approx 142.7$) to ensure numerical convergence. Finally, one can notice that no instability is observed for $R_{grid} \leqslant 34$, i.e. when the grid is too coarse.

The typical time step is of the order $\Delta t = 5 \times 10^{-3}$, and the integration time $t_{max} \approx 750$. The time step was systematically chosen such that the Courant–Friedrichs–Lewy (CFL) number remained smaller than 0.9 during the entire computation. The simulations were carried out using 64 central processing units (CPUs) on the Cray-XE6 machine 'Monte Rosa' of the Swiss Supercomputing Centre (CSCS).

4.2. *Numerical validation of the forced two-dimensional basic flow*

Here, we investigate how to easily establish the basic flow (2.8). An obvious choice would be to solve the Navier–Stokes equations in an inertial frame of reference, in a domain bounded by a streamline, and to impose a boundary velocity $\boldsymbol{u}_{bnd} = \nabla \times (\Psi \boldsymbol{e}_z)$. However, this would require a numerical technique that can take into account a moving boundary, such as the arbitrary Lagrangian–Eulerian method. Moreover, this numerical approach does not have a simple experimental counterpart. Therefore, we have considered two alternatives that are expected to generate the basic flow (2.8) in the bulk. A first possible realization is the one of a librating rigid container whose boundary takes the form of a streamline of the basic flow. An ingenious, but somewhat more complex, alternative to obtain streamline deformation was devised by Eloy *et al.* (2003) for steady rotation along deformed streamlines. They performed experiments in

a cylindrical container, deformed by the compression of two or three rollers. To extend this approach towards libration mechanical forcing, one can librate the rollers while rotating the container at constant speed. In both cases, the dynamics of the system is most easily expressed in the librating frame of reference attached to the deformation, because the boundary is stationary in this frame. As such, the flow is governed by the equations (2.5) and (2.6). However, in the former case the boundary condition is $\boldsymbol{u}_{bnd} = \boldsymbol{0}$, whereas in the latter case it is $\boldsymbol{u}_{bnd} = -\varepsilon \cos(\omega t)\,\boldsymbol{e}_z \times \boldsymbol{e}_n$, where $\boldsymbol{e}_n$ denotes the outward unit normal vector of the boundary. To assess if the basic flow is correctly established, we consider the following error estimate:

$$\mathscr{E}(C) = \frac{\displaystyle\int_0^T \int_{C > -r^2/2} \|\boldsymbol{u} - \boldsymbol{U}\|^2 \, \mathrm{d}\boldsymbol{r} \, \mathrm{d}t}{\displaystyle\int_0^T \int_{C > -r^2/2} \|\boldsymbol{U}\|^2 \, \mathrm{d}\boldsymbol{r} \, \mathrm{d}t}, \qquad (4.9)$$

where the integration is performed within a domain enclosed by a contour $C = \mathrm{const}$. This expression can be interpreted as follows: it is the relative *L*2 error norm of the deviation between the numerically established flow and the exact basic flow (2.8), within a domain bounded by a streamline of (2.8), time-averaged over an interval T of 10 libration periods. We have evaluated $\mathscr{E}(C)$ for 20 equidistant values of C in the interval [0.025, 1]. In figure 10, we show $\mathscr{E}$ for the two considered cases (librating rigid container, and librating rollers on a deformable container rotating at constant speed) and for several values of p.

We see that $\mathscr{E}(C)$ remains small for both forcing mechanisms and for all investigated values of p, except in a viscous boundary layer that emerges to accommodate the difference between the bulk flow (close to the exact basic flow) and the boundary velocity $\boldsymbol{u}_{bnd}$. The thickness of these viscous layers is (Wang 1970)

$$\delta = \sqrt{2E\omega^{-1}}. \qquad (4.10)$$

We assume that the velocity matching in this layer (between the bulk and the wall) is of the form of $1 - \exp(r^*\delta^{-1})$, where $r^* = r - F(\theta)$ denotes the distance from the wall. The boundary-layer correction should thus remain smaller than 1 % outside an annular-like region where $r^*\delta^{-1} < -\log(0.01) \approx 4.6$. This distance is indicated by a dashed axial line in figure 10. The excellent agreement within the bulk is also confirmed in figure 11, which compares the exact basic flow and the numerical solutions at time $t = M\pi/\omega$ with M an integer, i.e. when the basic flow has maximum strength. Moreover, M is such that we are beyond the spin-up regime, i.e. such that $t > 5E^{-1/2}$. Comparing both realizations, we find that the discrepancy between the established and basic flow within the boundary layer is considerably larger in the case of a rigid container. This can be explained as follows. For the case of a deformable container, the boundary velocity of the system with rollers is much closer to the exact basic flow (2.8). We thus expect viscous effects to be much less important. Hence, the discrepancy $\mathscr{E}$ is much smaller near the walls than when a rigid container is used to establish the desired basic flow.

Nevertheless, as the bulk flow in both realizations is very close to (2.8), all the theoretical results obtained in § 3 are valid in both cases. In the following, we will only consider the case of a rigid container because of its experimental convenience.
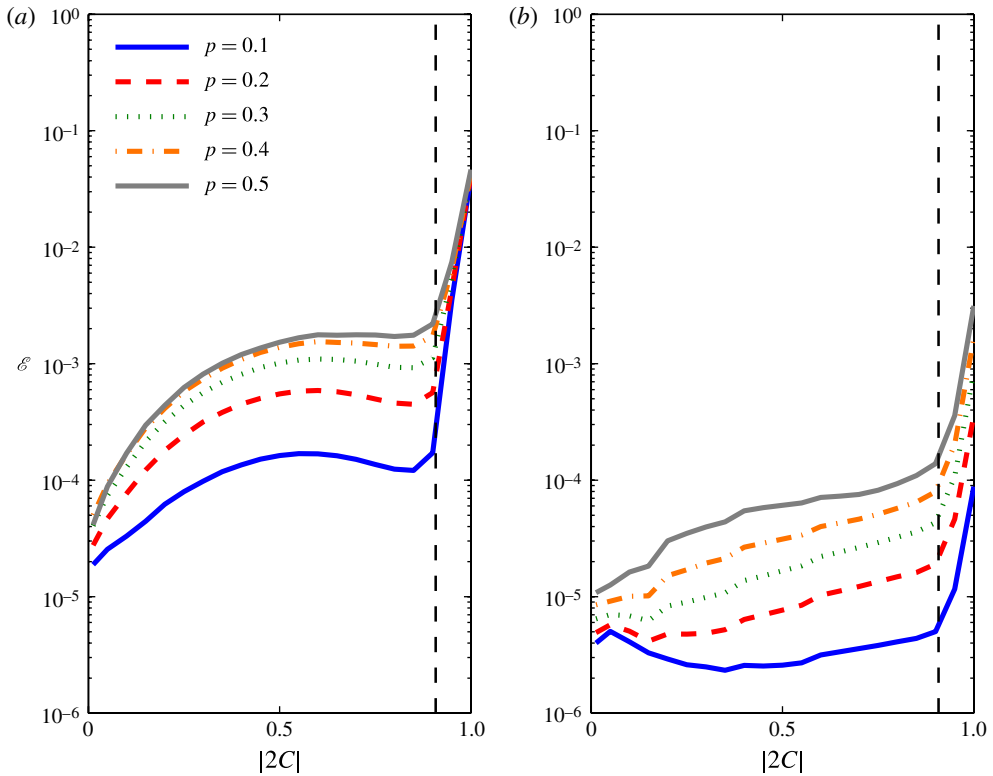
FIGURE 10. (Colour online) Relative $L2$ error norm $\mathscr{E}$ between the established flow and the exact basic flow (2.8), for the case of (*a*) a rigid librating container and (*b*) a rotating container deformed by librating rollers. Parameters: $n = 3$, $E = 5 \times 10^{-4}$, $\varepsilon = 1.0$ and $\omega = 2.5$. The dashed vertical line indicates a distance of 4.6δ, with $\delta = \sqrt{2E\omega^{-1}}$ the thickness of the viscous layer, for which the theoretical boundary-layer correction should be smaller than $1\,\% \approx \exp(-4.6)$.

4.3. *Onset and development of the LDMI*

In this section, we discuss 3D nonlinear simulations of the libration-driven tripolar instability. The simulation domain is a cylinder that is periodic in the z direction with a tripolar cross-section (in the x–y plane) like the ones discussed in the previous section. Furthermore, we keep the aspect ratio h between the height of the cylinder and the mean radius of the cross-section fixed at a value of 2. The choice of periodic boundary conditions is motivated by the fact that we avoid the presence of thin Ekman layers at the top and bottom of the cylinder, which have two important drawbacks. (i) They are at the origin of 3D flows, even before the multipolar instability emerges. (ii) The proper numerical resolution of these layers would lead to a considerable increase in CPU time.

We will first present some general features of this instability. Then, we will validate the theoretical results obtained in §3 through a systematic study of the dependence of the viscous growth rate σ_v on the flow parameters E, ω, p and ε. Finally, as numerical simulations allow us to go beyond the linear theory, we will investigate two characteristics of the nonlinear regime that are of interest, namely the amplitude and viscous dissipation of the instability at saturation.
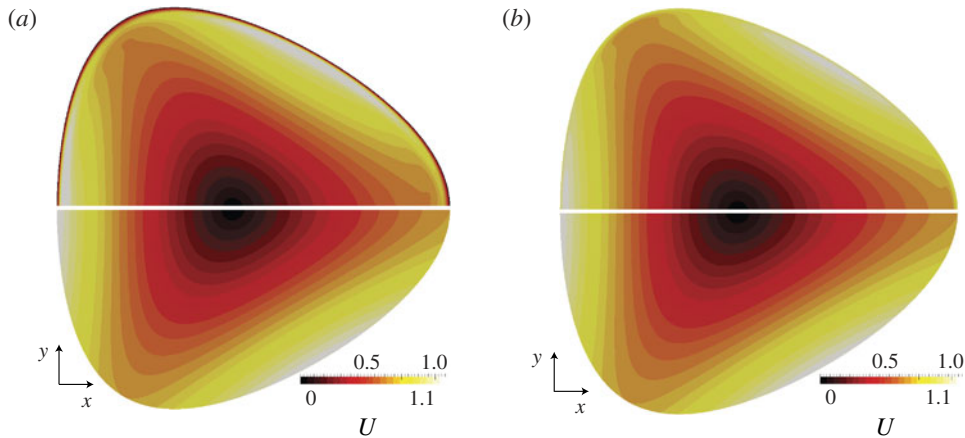
FIGURE 11. (Colour online) Comparison for $n = 3$, $p = 0.3$, $E = 5 \times 10^{-4}$, $\omega = 2.5$ and $\varepsilon = 1$ between the exact basic flow (2.8) (bottom half) and the numerically established 2D basic flow (top half) for the case of (*a*) a rigid tripolar ($n = 3$) container and (*b*) a deformable container, deformed by rollers.

4.3.1. *General characteristics of the LDMI flows*

The basic flow being 2D, and the stability analysis showing instability for 3D perturbations, we can expect that the axial kinetic energy E_z,

$$E_z = \frac{1}{2} \int_V u_z^2 \, \mathrm{d}V, \tag{4.11}$$

is a good proxy for the development of the instability (V being the volume of the container). Figure 12(*a*,*b*) shows typical time series of E_z, which exhibit three distinct stages. Until $t \approx 40$, E_z is negligibly small, and hence the basic flow is virtually 2D. From $t \approx 40$, the axial kinetic energy undergoes exponential growth over many decades. During this stage, u_z has a wavy structure, as highlighted by a snapshot of u_z at $t = 80$ (see figure 12*c*). Eventually E_z saturates at a value of approximately 0.08 around $t \approx 110$. In the last stage, E_z exhibits chaotic intermittent behaviour, which is related to the appearance of small-scale turbulence; this is illustrated in figure 12(*d*) by the snapshot of u_z at $t = 160$. The turbulence is space-filling, and is thus not related to the presence of a boundary-layer instability. This contrasts with previous studies of libration-driven flows in axisymmetric containers (Noir *et al.* 2009, 2010; Calkins *et al.* 2010; Sauret *et al.* 2012), where the observed turbulence was triggered by a Taylor–Görtler instability and remained limited to the near-wall region.

4.3.2. *Thresholds and viscous growth rates of the LDMI*

We now investigate systematically how ε, p, ω and E affect the growth rate σ_v of the instability. Libration frequencies $\omega < 2$ are left out of consideration to avoid any direct forcing of inertial modes. Note, however, that the LDMI is nevertheless expected for $\omega < 2$, as shown by figure 6. In order to extract growth rates from time series of the axial kinetic energy E_z such as the ones plotted in figure 12(*a*,*b*), we proceed as follows. First, we use a moving average procedure to filter out the frequency component at 2ω from E_z. Subsequently, we fit a function of the form $A \exp(2\sigma_v t) + B$ to the filtered signal within a certain time window $[t_1, t_2]$. The growth rates σ_v obtained in this way are slightly dependent on the choice of t_1 and t_2. For the
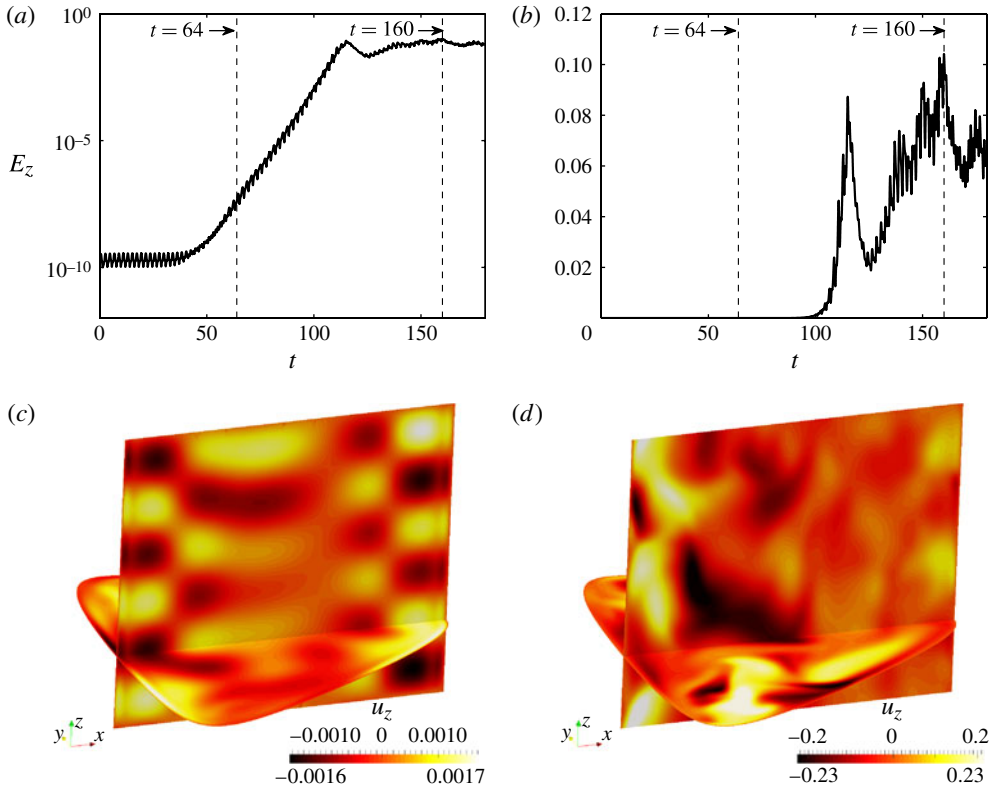
FIGURE 12. (Colour online) Time series of the axial kinetic energy E_z in a 3D numerical simulation of the LDMI for $n = 3$, $\omega = 3$, $\varepsilon = 1$, $p = 0.45$ and $E = 5 \times 10^{-4}$, on both (*a*) a logarithmic scale, illustrating the exponential growth, and (*b*) a linear scale, giving evidence of the subsequent intermittent behaviour. Snapshots of u_z during (*c*) the exponential growth stage at $t = 64$, and (*d*) the intermittency stage at $t = 160$.

robustness of the results, we have repeated the procedure described above for several choices of t_1 and t_2. In the following figures, the growth rates displayed correspond to the mean of the measured values, whereas the error bars indicate the maximum and the minimum value.

The thick solid lines in figure 13 show the (inviscid) asymptotic WKB formula (3.16) for $C = -1/2$ (boundary pathline), whereas each of the crosses or thin lines represents a (viscous) resonance between a pair of inertial modes. Finally, the grey circles (red online) correspond to the numerically obtained growth rates, and are in good agreement with the values of σ_v of the most unstable resonances. The slight numerical discrepancy between the simulations and global analysis may be attributed to the following two factors: (i) the global theory is, strictly speaking, only valid in the limit $\varepsilon p \ll 1$; and (ii) the seed perturbation on which the instability grows consists of pure numerical noise, which implies that we do not control whether inertial modes are equally represented within this seed perturbation. As such, the most unstable resonance does not necessarily dominate at the onset of instability and during its initial exponential growth. Finally, we see that the asymptotic WKB analysis provides a correct upper bound for the growth rates, but the results are not close to this bound.
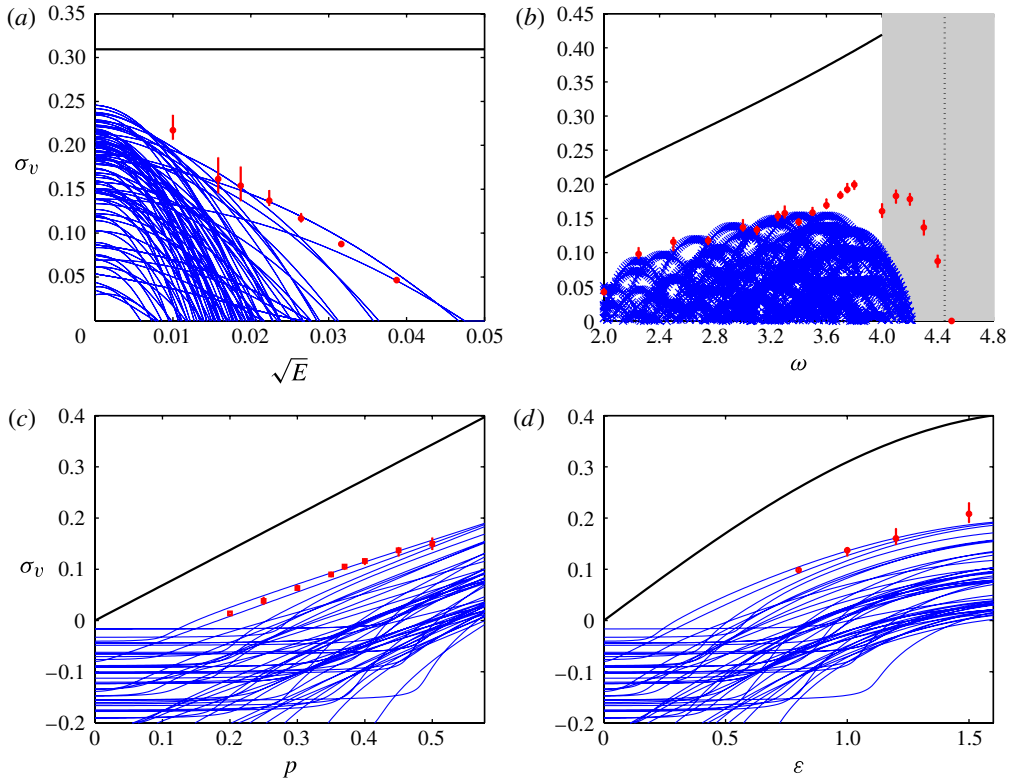
FIGURE 13. (Colour online) Growth rate σ_v as a function of the flow parameters E, p, ε and ω for $n = 3$. Results of the asymptotic WKB analysis (thick black line) given by (3.16) for $C = -1/2$ (boundary pathline), global analysis (thin lines and crosses; blue online) and numerical simulations (circles; red online): (*a*) as a function of E for $\varepsilon = 1$, $p = 0.45$ and $\omega = 3$; (*b*) as a function of ω for $\varepsilon = 1$, $p = 0.45$ and $E = 5 \times 10^{-4}$; (*c*) as a function of p for $\omega = 3$, $\varepsilon = 1$ and $E = 5 \times 10^{-4}$; and (*d*) as a function of ε for $\omega = 3$, $p = 0.45$ and $E = 5 \times 10^{-4}$.

This is naturally due to the fact that the WKB theory is an inviscid theory, whereas the range of Ekman numbers under consideration is not asymptotically small. Note also that we represent in figure 13 the maximum local inviscid WKB growth rate, which is reached on the boundary pathline ($C = -1/2$), i.e. in a zone dominated by viscosity (viscous boundary layer) in the simulations. The growth rate provided by the local stability analysis can thus only be an upper bound. Nevertheless, we observe that the WKB captures reasonably well the trend of the dependence of σ_v on ω, ε and p.

Figure 13(*b*) shows us that the instability tends to disappear for $\omega > 4$. Indeed, the LDMI is the result of parametric resonances of inertial waves that do not exist for $\omega > 4$ at zeroth order in ε and p: this is the forbidden zone (see § 3.1.3). Note that the finite values of εp force us to consider the first order in εp, which gives a forbidden zone for $\omega > 4 + \varepsilon p$, as in Le Dizès (2000). The global analysis and the numerical simulations give evidence of the existence of resonant frequencies around which the growth rate peaks as, for example, at $\omega = 3$, as already observed by Cébron *et al.* (2012*c*). Near $\omega = 3.75$, there is some disagreement between the global theory and the simulations. The increased growth rates in this frequency range are due to
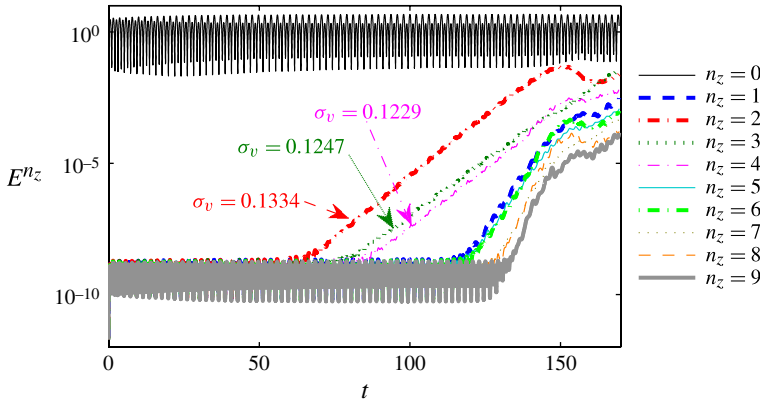
FIGURE 14. (Colour online) Time series of the axial Fourier components $n_z = 0$–9 of the total kinetic energy for $n = 3$, $\omega = 3$, $p = 0.45$, $\varepsilon = 1$ and $E = 5 \times 10^{-4}$. Numerically obtained growth rates for the components $n_z = 2, 3, 4$ are shown in the figure (and can be compared with the values given in figure 7(b), i.e. $\sigma_v = 0.136$ for $n_z = 2$ and $\sigma_v = 0.127$ for $n_z = 3$).

the proximity of the forbidden zone, which leads to numerous resonances involving higher-order inertial modes, as already seen in Le Bars *et al.* (2010) for instance. Hence, these become increasingly difficult to capture in the global analysis.

We can furthermore decompose the flow into its Fourier components (along the z direction),

$$\boldsymbol{u}(\boldsymbol{r}, t) = \sum_{n_z=-\infty}^{\infty} \boldsymbol{U}_{n_z}(x, y, t)\, e^{i n_z z}, \tag{4.12}$$

and consider the energies $E^{n_z}(t)$ associated with these modes,

$$E^{n_z}(t) = \frac{1}{2} \iint \boldsymbol{U}_{n_z}^2(x, y, t) + \boldsymbol{U}_{-n_z}^2(x, y, t)\, \mathrm{d}x\, \mathrm{d}y. \tag{4.13}$$

Figure 14 shows the time evolution of the different components E^{n_z} for $\omega = 3$, $p = 0.45$, $\varepsilon = 1$ and $E = 5 \times 10^{-4}$. We observe resonances that are associated with axial wavenumbers $n_z = 2, 3, 4$. Note that multiple resonances may coexist for each single value of n_z, which leads to a simultaneous growth of all the resonances. The growth rates σ_v corresponding to $n_z = 2, 3, 4$ are displayed as well. For $n_z = 2, 3$, these are in excellent agreement with the theoretically predicted growth rates given in figure 7(b). However, we also find a resonance for $n_z = 4$. Finally, we see that, for $t \gtrsim 120$, the flow contains a broad range of axial wavenumbers. This is a clear signature of the emergence of nonlinear effects and the generation of turbulence observed in figure 12(d).

4.3.3. *Amplitude of the flow driven at saturation*

We have shown previously (see e.g. figure 12d) that the LDMI may generate vigorous flows that contain a broad range of length scales. An important measure of this regime is the amplitude $\mathscr{A}$ of the flow, defined by

$$\mathscr{A}(t) = \sqrt{V_{bulk}^{-1} \iiint_{V_{bulk}} (\boldsymbol{u} - \boldsymbol{U})^2\, \mathrm{d}V}. \tag{4.14}$$
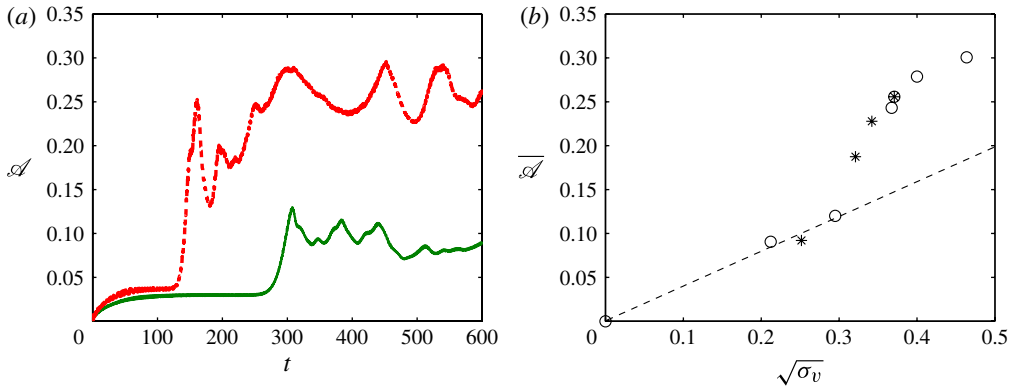
FIGURE 15. (Colour online) Amplitude of the LDMI for $n = 3$, $\omega = 3$ and $\varepsilon = 1$. (a) Time series of $\mathscr{A}$ (see definition in (4.14)) for $p = 0.3$, $E = 5 \times 10^{-4}$ and $p = 0.45$, $E = 2.5 \times 10^{-4}$ (dashed line). (b) Time-averaged amplitudes $\overline{\mathscr{A}}$ against growth rates σ_v for $p = 0.45$ and $E = 2.5 \times 10^{-3}$, 1.5×10^{-3}, 1×10^{-3}, 7×10^{-4}, 5×10^{-4}, 2.5×10^{-4} and 1×10^{-4} ($\bigcirc$) and $E = 5 \times 10^{-4}$ and $p = 0.3$, 0.37, 0.4, 0.45 ($*$). Linear fit through the four leftmost data points with a slope of 0.40 (dashed line).

This definition is based on the following considerations. The amplitude of the instability is related to the difference between the total driven (unstable) flow $\boldsymbol{u}$ and the exact (laminar) basic flow $\boldsymbol{U}$. However, as we have shown in §4.2, important differences between $\boldsymbol{u}$ and $\boldsymbol{U}$ exist before the instability sets in due to the boundary viscous layers. To discard the effect of these boundary layers, we limit the integration domain to a volume V_{bulk} that only contains points for which $C(r, \theta) > -(1 - 5\delta)^2/2$.

In figure 15(a), we show time series of $\mathscr{A}(t)$ for the following parameter sets: $n = 3$, $\omega = 3$, $p = 0.30$, $\varepsilon = 1$, $E = 5 \times 10^{-4}$; and $n = 3$, $\omega = 3$, $p = 0.45$, $\varepsilon = 1$, $E = 2.5 \times 10^{-4}$. In both cases, we can identify three distinct stages. Prior to the presence of the LDMI, $\mathscr{A}(t)$ is almost constant and remains smaller than 0.05. Then, $\mathscr{A}(t)$ increases exponentially, and evolves in a complex way. Eventually, $\mathscr{A}(t)$ reaches a saturated state, in which it fluctuates around some time-averaged value.

To study the effect of the flow parameters more systematically, we consider temporal averages $\overline{\mathscr{A}}$ of $\mathscr{A}(t)$, where the averaging interval typically consists of 150–200 time units. For the values $E = 10^{-4}$ to 2.5×10^{-3} considered, this corresponds at least to 1.5 spin-up times. In figure 15(b), we display $\overline{\mathscr{A}}$ against $\sigma_v^{1/2}$ for a large number of parameter combinations. We observe that

$$\overline{\mathscr{A}} \approx 0.4\sigma_v^{1/2} \tag{4.15}$$

for $\sigma_v^{1/2} \lesssim 0.3$. This finding is consistent with previous studies of the nonlinear evolution of the elliptical instability (e.g. Mason & Kerswell 1999; Lacaze *et al.* 2004; Cébron *et al.* 2010a), and, in a more general sense, the theory of supercritical pitchfork instabilities. In these previous studies, it was possible to define a single control parameter κ that governs the onset of instability. It has been observed that, close to threshold, the amplitude scales as $(\kappa - \kappa_c)^{1/2}$, where κ_c is the critical value for the onset of instability. In our present study, we may thus interpret σ_v as equivalent to $\kappa - \kappa_c$. This indeed seems justified, as both measures are proxies for the distance from threshold.
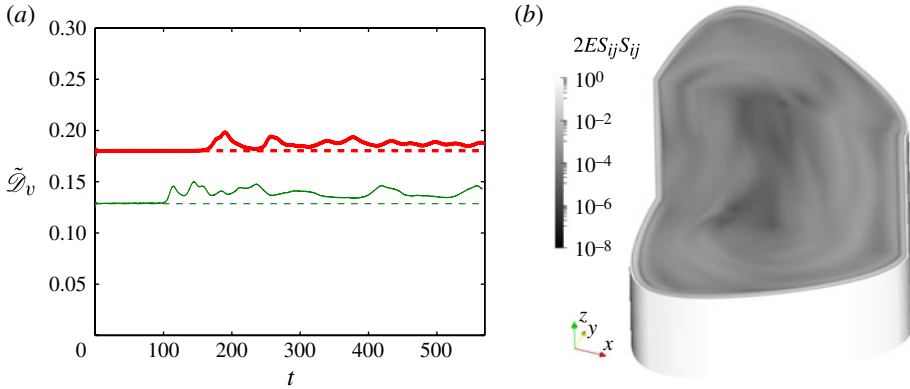
FIGURE 16. (Colour online) (*a*) Moving-average $\tilde{\mathscr{D}}_v$ of the viscous dissipation of the flow for $n = 3$, $\omega = 3$, $\varepsilon = 1$, $p = 0.4$, $E = 5 \times 10^{-4}$ (thick) and $p = 0.45$, $E = 2.5 \times 10^{-4}$ (thin). Dashed lines indicated the average dissipation $\mathscr{D}_v^L$ of the laminar base state. (*b*) Snapshot of the local viscous dissipation rate $2ES_{ij}S_{ij}$ for $n = 3$, $\omega = 3$, $\varepsilon = 1$, $p = 0.4$, $E = 5 \times 10^{-4}$ at $t = 424$.

For larger values of σ_v, this simple scaling law does not hold any more. This is in agreement with Kerswell (2002), who argues that the primary instability only saturates and is stable for a small range of parameters near the threshold. Finally, we also observe that $\overline{\mathscr{A}}$ tends to saturate to a maximum value of approximately 0.3 for $\sigma_v^{1/2} \gtrsim 0.45$.

4.3.4. *Viscous dissipation of the instability*

The viscous dissipation rate $\mathscr{D}_v$ is defined by

$$\mathscr{D}_v = 2E \iiint S_{ij} S_{ij} \, \mathrm{d}V, \tag{4.16}$$

where $S_{ij} = (\nabla u + \nabla u^{\mathrm{T}})/2$ is the strain-rate tensor. This quantity, however, is strongly oscillating, and therefore we show in figure 16(*a*), for two sets of parameters, a moving average of $\mathscr{D}_v$ with an averaging window of two libration periods, and denote it $\tilde{\mathscr{D}}_v$. Clearly, even before the onset of instability, $\tilde{\mathscr{D}}_v$ takes significant values and is constant. The dissipation in this stage is mainly due to the presence of viscous boundary layers. In appendix C, we have modelled this dissipation with a simple theoretical model based on the boundary-layer theory of Wang (1970). This model shows reasonable agreement with simulation results of the laminar base state. We denote this dissipation of the laminar flow $\mathscr{D}_v^L$ and indicate its average value by a dashed line in figure 16(*a*). After the onset of instability, the dissipation slightly increases. In figure 16(*b*), we show a snapshot of the local viscous dissipation rate $2ES_{ij}S_{ij}$ at $t = 424$ for the case $n = 3$, $\omega = 3$, $\varepsilon = 1$, $p = 0.4$ and $E = 5 \times 10^{-4}$. As can be seen, the dissipation rate is up to three orders of magnitude larger in the boundary-layer region. Since the volume fraction occupied by this region is of the order of $E^{1/2} \approx 0.022$, we expect that boundary-layer contributions will also dominate the total viscous dissipation rate in the nonlinear regime.

We may now define the dissipation due only to the instability $\mathscr{D}_v^I$ as

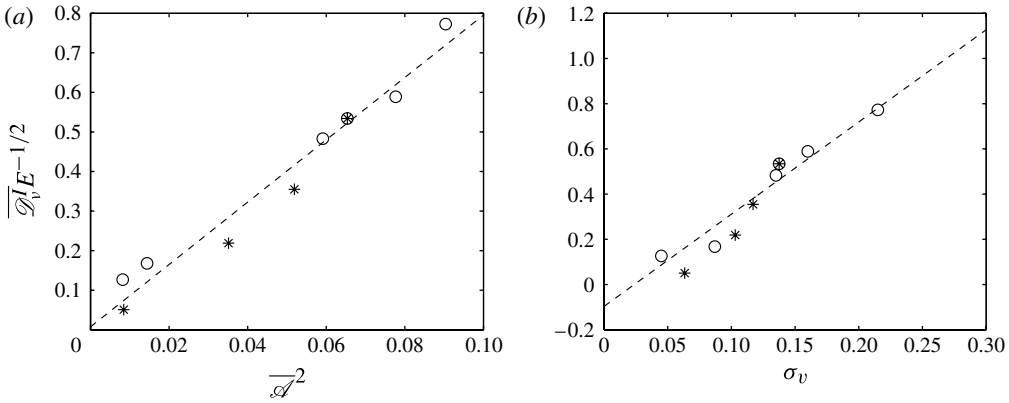$$\mathscr{D}_v^I = \mathscr{D}_v - \mathscr{D}_v^L. \tag{4.17}$$

FIGURE 17. Evolution of the viscously rescaled dissipation $E^{-1/2}\overline{\mathscr{D}_v^I}$ for $n = 3$, $\omega = 3$, $\varepsilon = 1$, $p = 0.45$ and $E = 1.5 \times 10^{-3}$, 10^{-3}, 7×10^{-4}, 5×10^{-4}, 2.5×10^{-4}, 10^{-4} ($\bigcirc$) and $p = 0.3$, 0.37, 0.4, 0.45, $E = 5 \times 10^{-4}$ ($*$), dashed lines being linear fits to the data points: (a) as a function of $\overline{\mathscr{A}}^2$, i.e. the square of the amplitude of the equilibrated flow driven by the LDMI; and (b) as a function of the growth rate σ_v.

As for the amplitude of the instability (see § 4.3.3), we now consider time averages of $\mathscr{D}_v^I$ over long time intervals in the saturated nonlinear regime, and investigate how this quantity scales with respect to other characteristics of the instability. In figure 17, we find that $\overline{\mathscr{D}_v^I}$ scales as

$$\overline{\mathscr{D}_v^I} \approx 7.8 \, \overline{\mathscr{A}}^2 \sqrt{E}. \tag{4.18}$$

This scaling law is in agreement with previous studies (e.g. Williams *et al.* 2001; Le Bars *et al.* 2011), and is consistent with (4.16). Indeed, as the viscous dissipation is quadratic in the velocity, we also expect it to scale quadratically in $\overline{\mathscr{A}}$. Since we have established previously that, close to the threshold, $\overline{\mathscr{A}}$ scales as $\sigma_v^{1/2}$, we expect $\overline{\mathscr{D}_v^I} \propto \sigma_v \sqrt{E}$. This is indeed the case, as illustrated in figure 17, where we see that all data points approximately collapse onto a straight line given by

$$\overline{\mathscr{D}_v^I} \approx 4.1 \sigma_v \sqrt{E}. \tag{4.19}$$

It is remarkable that the viscous growth rate, a result of the linear stability analysis, is still a relevant parameter to characterize the nonlinear regime. It may indicate that the nonlinear regimes we have explored are not very far from the instability threshold.

4.4. *LDMI, a generic instability (simulation in a spherical geometry)*

Because of its possible geophysical relevance and to show that the LDMI is a generic mechanism, we now investigate numerically whether the libration-driven tripolar instability can also take place in deformed spherical containers. We thus consider a spherical container, and move each point of its boundary at a cylindrical radius r towards a point at the cylindrical radius r' following

$$r' = \left[1 + \frac{p}{n} \cos(n\theta)\right] r, \tag{4.20}$$

in each plane perpendicular to the rotation axis (using here $n = 3$). This deformation corresponds to a multipolar shape in the limit $p \ll 1$ (see (2.4)).
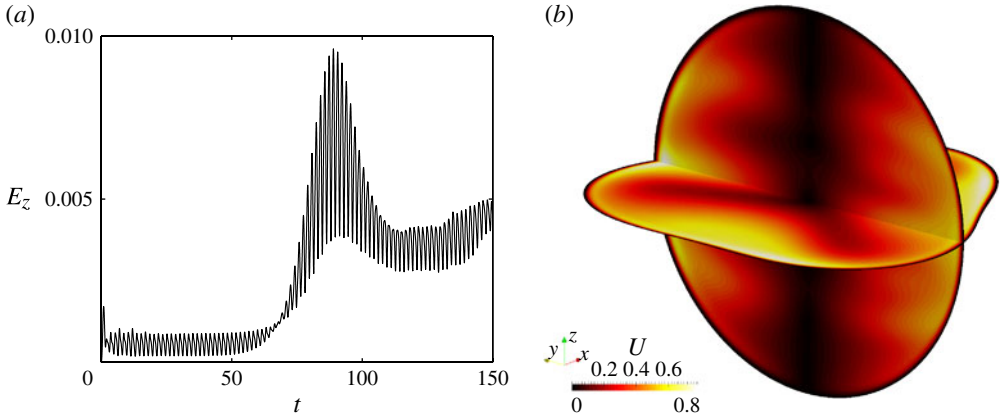
FIGURE 18. (Colour online) Libration-driven tripolar instability in a deformed spherical container for the parameters $p = 0.25$, $E = 5 \times 10^{-4}$, $\omega = 3.8$ and $\varepsilon = 1$: (*a*) time series of axial kinetic energy and (*b*) 3D snapshot of the velocity magnitude at $t = 84$.

Figure 18 displays results of a simulation for parameters $n = 3$, $p = 0.25$, $\omega = 3.8$, $\varepsilon = 1$ and $E = 5 \times 10^{-4}$, which are values of the same order of magnitude as the ones used in previous sections on cylindrical geometry. In figure 18(*a*), the time series of the axial kinetic energy (4.11) again exhibits three distinct stages. Prior to the onset of instability (for $t < 60$), E_z oscillates around a small but non-negligible value of 0.001. The corresponding velocity component u_z is related to the Ekman pumping due to the viscous Ekman layers. Starting from $t \approx 60$, E_z undergoes an exponential growth over a short time interval (until $t \approx 90$): an LDMI is thus excited. Further evidence for this is given in figure 18(*b*), where we observe that the velocity magnitude $\|\boldsymbol{u}\|$ is characterized by an oscillatory spatial pattern in the bulk of the fluid. Moreover, we find that the growth rate of the instability is $\sigma_v \approx 0.108$. We can compare this value to the corresponding values for cylindrical geometry, shown in figure 13(*b*). For $p = 0.45$ and all other parameters equal to those in the present spherical case, we find that the growth rate in cylindrical geometry is $\sigma_v \approx 0.2$. Hence, for $p = 0.25$, we can estimate a growth rate that is approximately $0.2 \times 0.25/0.45 \approx 0.111$, which is in good agreement with the measured value of $\sigma_v \approx 0.108$. We can thus conclude that the LDMI, as a local instability, can be excited in any geometry with a non-zero multipolar component in its cross-section if the ratio $\varepsilon p/E$ is large enough.

5. Conclusion and discussion

Given the planetary relevance of libration-driven flows, a number of studies have been devoted to librating axisymmetric containers in order to investigate the role of the viscous coupling (e.g. Noir *et al.* 2009, 2010, 2012; Busse 2010*a*,*b*; Calkins *et al.* 2010; Sauret *et al.* 2010, 2012). These works show that, in this case, libration does not lead to significant power dissipation or angular momentum transfer. As shown by Cébron *et al.* (2012*c*), these conclusions should be re-addressed in elliptical containers, since space-filling turbulence may be observed in numerical and laboratory experiments. In this work, we have shown that this space-filling turbulence is actually due to a particular case of a generic instability, the LDMI, which can be excited in any librating non-axisymmetric container. For instance, in librating synchronized moons

(see e.g. Noir *et al.* (2012) for details), the Ekman numbers of fluid layers are so small ($E = 10^{-12}$–10^{-10}) that an LDMI can be expected, even if the libration amplitudes and the deformations are very small ($p = 10^{-5}$–10^{-3}, $\varepsilon = 10^{-5}$–10^{-3}, depending on the compressibility of the fluid and the rigidity of the solid layer). This may question the usual spherical geometry approximation used to study planetary flows numerically.

In the present study, we have first performed a short-wavelength Lagrangian local stability analysis of the basic flow. This has allowed us to compute the inviscid growth rates of the LDMI for arbitrary deformations and libration amplitudes. Then, in the limit of small deformations, we have obtained an analytical expression for the growth rate using a multiple-scale analysis, and we have successfully compared it to the exact stability results. This local stability analysis shows that the LDMI can be excited as soon as a flow periodic trajectory has a multipolar shape.

To complete our understanding of the LDMI, we have then carried out a global stability analysis, which allows us to take confinements and viscous effects into account, and thus to predict accurate onsets of the LDMI. This analysis has shown that the LDMI can also be seen as the parametric resonance between two inertial waves of a rotating fluid and a librating multipolar strain (which is not an inertial wave or mode). Seldom compared in the literature, we have shown that the local and the global stability results are consistent and lead to similar growth rates in the inviscid limit.

Numerical simulations are then used to demonstrate the existence of the LDMI in librating systems. After confirming that the considered basic flow is indeed established in the bulk of librating multipolar containers, we have systematically compared the simulations with the theoretical stability results. The quantitative agreement between the two is excellent, even for the details of simultaneous growths of several parametric resonances of inertial waves. The simulations are then used to explore the nonlinear regimes of the LDMI, which are difficult to describe theoretically. This allows us to confirm that, in the equilibrated state, LDMI-driven flows are of significant amplitude, which are almost of the same order of magnitude as the basic flow, as previously observed for the elliptical instability (e.g. Cébron *et al.* 2010*a*). Subsequently, the viscous dissipation of the libration-driven flows is carefully quantified and compared with previously established scaling laws. Finally, we confirm that the LDMI is a generic instability by showing one simulation of the excitation of the instability in a spherical container deformed with a multipolar shape.

To conclude, we would like to point out that the experimental set-up needed to study the LDMI may be one of the simplest of those devoted to inertial instabilities. Indeed, we do not need deformable containers (as in Eloy *et al.* (2003) for the study of elliptical or triangular instabilities) or two motors (as in Lagrange *et al.* (2011) for the study of the precessional instability). To study the LDMI experimentally, only a rigid deformed container and a rotating table are needed. The range of parameters where the instability is excited is easy to reach: considering, for instance, a small tripolar cylinder with a radius $R = 15$ cm, a height $H = 30$ cm and a deformation $p = 0.45$, slowly rotating at 0.9 r.p.m. and librating with a period of 22 s, an LDMI is excited as soon as the libration angle is larger than $6°$ (any larger rotation rate would be strongly destabilizing). Then, in spite of its simplicity, such a set-up easily allows, via the LDMI, the generation of strong 3D space-filling flows within a rigid container.

Acknowledgements

Supplementary materials

Supplementary materials are available at http://dx.doi.org/10.1017/jfm.2013.623.

Appendix A. Local and global stability analysis: details

A.1. *Asymptotic local stability analysis for small forcings $\varepsilon p \ll 1$*

Assuming that the product $\varepsilon p \ll 1$ remains small, we first calculate the trajectory in the inertial frame. At leading order, we obtain the circular trajectory $X^{(0)}(t)$ due to the solid-body rotation. For a given initial position, e.g. $(R, 0)$, $X^{(0)}(t)$ can be written as

$$X^{(0)} = R\cos(t)\,e_x + R\sin(t)\,e_y. \tag{A 1}$$

This allows one to obtain the deviations $X^{(1)}(t)$ induced by the multipolar deformation:

$$X^{(1)}(t) = \frac{R^{n-1}}{2\,\omega}[\cos((\omega - 1)t) - \cos((\omega + 1)t)]\,e_x$$
$$+ \frac{R^{n-1}}{2\,\omega}[\sin((\omega - 1)t) - \sin((\omega + 1)t)]\,e_y. \tag{A 2}$$

With this, one can evaluate ∇U on the perturbed trajectory, up to order $O(\varepsilon p)$, allowing one to solve for the wavenumber $\mathcal{K}(t)$. At lowest order, we obtain $\mathcal{K}^{(0)}(t)$, given in § 3.1.3, which allows one to obtain the next order:

$$\mathcal{K}^{(1)}(t) = \frac{(n - 1)R^{n-2}}{2\,\omega}[\cos((\omega + 1)t - \phi) - \cos((\omega - 1)t + \phi)]\,e_x$$
$$+ \frac{(n - 1)R^{n-2}}{2\,\omega}[\sin((\omega + 1)t - \phi) + \sin((\omega - 1)t + \phi)]\,e_y. \tag{A 3}$$

Note that we recover the expressions for $X(t)$ and $\mathcal{K}(t)$ given in the appendix of Herreman *et al.* (2009) by considering the particular case they study, i.e. $n = 2$ and $\omega = 1$.

A.2. *Global stability analysis*

A.2.1. *Definition of operators*

In the global stability analysis, we have used the operators

$$\mathscr{L} = \begin{bmatrix} \partial_t & -2 & 0 & \partial_r \\ 2 & \partial_t & 0 & r^{-1}\partial_\theta \\ 0 & 0 & \partial_t & \partial_z \\ \partial_r + r^{-1} & r^{-1}\partial_\theta & \partial_z & 0 \end{bmatrix}, \tag{A 4}$$

$$\mathcal{N} = \mathrm{i} \begin{bmatrix} D_1 - (n-1)r^{n-2} & -\mathrm{i}(n-2)r^{n-2} & 0 & 0 \\ -\mathrm{i}nr^{n-2} & D_1 + (n-1)r^{n-2} & 0 & 0 \\ 0 & 0 & D_1 & 0 \\ 0 & 0 & 0 & 0 \end{bmatrix}, \tag{A 5}$$

$$\mathcal{V} = \begin{bmatrix} D_2 - r^{-2} & -2\,r^{-2}\partial_\theta & 0 & 0 \\ 2\,r^{-2}\partial_\theta & D_2 - r^{-2} & 0 & 0 \\ 0 & 0 & D_2 & 0 \\ 0 & 0 & 0 & 0 \end{bmatrix}, \tag{A 6}$$

$$\mathcal{I} = \begin{bmatrix} 1 & 0 & 0 & 0 \\ 0 & 1 & 0 & 0 \\ 0 & 0 & 1 & 0 \\ 0 & 0 & 0 & 0 \end{bmatrix}, \tag{A 7}$$

with

$$D_1 = -r^{n-1}\partial_r - \mathrm{i}r^{n-2}\partial_\theta, \quad D_2 = r^{-2}\partial_{rr}^2 + r^{-1}\partial_r + r^{-2}\partial_{\theta\theta}^2 + \partial_{zz}^2. \tag{A 8}$$

A.2.2. *Inviscid boundary condition correction induced by wall deformations*

The deformation of the cylindrical boundary introduces flow corrections, and it is necessary to account for these in the global stability calculation. To find these corrections, we express the kinematic boundary condition on the moving boundary as

$$\frac{\partial \zeta^R}{\partial t} + \boldsymbol{U}^R \cdot \boldsymbol{\nabla} \zeta^R + \boldsymbol{u}^R \cdot \boldsymbol{\nabla} \zeta^R|_{surface} = 0. \tag{A 9}$$

Here ζ^R is defined by (2.14) and the basic flow $\boldsymbol{U}^R$ is given by (2.13). The basic flow is such that this equation reduces to

$$\boldsymbol{u}^R \cdot \boldsymbol{\nabla} \zeta^R|_{surface} = 0. \tag{A 10}$$

We will now find an asymptotic form of this condition for small p, expressed at the unperturbed boundary surface $r = 1$. When $p \ll 1$, the lateral surface is written in cylindrical coordinates as the place where $r = r_s(\theta, t)$, with

$$r_s(\theta, t) = 1 + \frac{p}{n} \cos n(\theta + \Delta\varphi \sin \omega t) + O(p^2), \tag{A 11}$$

for $\theta \in [0, 2\pi]$. Taylor-expanding (A 10) around $r = 1$, we then get

$$u_r^R(1) = -p \left[\frac{1}{n} \cos n(\theta + \Delta\varphi \sin \omega t) \right] \partial_r u_r(1)$$
$$- p[\sin n(\theta + \Delta\varphi \sin \omega t)] u_\theta(1) + O(p^2) \tag{A 12}$$

which using (2.18) becomes

$$u_r^R(1) = p \left[\mathrm{e}^{\mathrm{i}n\theta} g(t) \left(-\frac{1}{n} \partial_r u_r(1) + \mathrm{i}u_\theta(1) \right) \right.$$
$$\left. + \mathrm{e}^{-\mathrm{i}n\theta} g^\dagger(t) \left(-\frac{1}{n} \partial_r u_r(1) - \mathrm{i}u_\theta(1) \right) \right] + O(p^2). \tag{A 13}$$

These $O(p)$ modifications of the radial velocity enter in the growth rate calculation through the boundary terms of the two equations that express the solvability

condition (3.35). Considering the form of the asymptotic ansatz (3.27), we have

$$Q_{1,4}^\dagger(1)Z_{1,1}(1) = pA_2 g_{-j}^\dagger \underbrace{\left[Q_{1,4}^\dagger(1) \left(-\frac{1}{n}\partial_r Q_{2,1}(1) - iQ_{2,2}(1) \right) \right]}_{\mathscr{B}_{12}}, \qquad \text{(A 14)}$$

$$Q_{2,4}^\dagger(1)Z_{2,1}(1) = pA_1 g_{+j} \underbrace{\left[Q_{2,4}^\dagger(1) \left(-\frac{1}{n}\partial_r Q_{1,1}(1) + iQ_{1,2}(1) \right) \right]}_{\mathscr{B}_{21}}. \qquad \text{(A 15)}$$

From a physical point of view, these boundary terms correspond to the power exchanged between two interacting modes (because of boundary deformations).

Appendix B. Explicit streamlines parametrization for $n = 3$

For the case of the tripolar and quadrupolar basic flows, the streamlines defined by the streamfunction (2.8) can be expressed as an analytic functional relationship between r and θ, i.e. $r = F(\theta)$. We have used this formulation in our numerical approach to generate a grid whose boundary coincides with the shapes of the streamlines (see § 4.1) $\Psi \equiv C$. We have chosen the value of C such that the boundary contour tends to the unit circle as p goes to zero, i.e. $C = -1/2$:

$$\Psi = -\frac{r^2}{2} + p\frac{r^3}{3}\cos(3\theta) = -\frac{1}{2}. \qquad \text{(B 1)}$$

This implicitly defines $r = F(\theta)$, and can be recast as a cubic equation for r,

$$\tau r^3 - r^2 + 1 = 0, \qquad \text{(B 2)}$$

where we have defined $\tau = 2p\cos(3\theta)/3$. This equation can only have positive roots for all values of θ if $\Delta = 4 - 27\tau^2 > 0$. This implies that $p \leqslant 1/\sqrt{3}$, which is equivalent to the condition $\beta_n \leqslant 1$ for $n = 3$ (see § 2). Upon the introduction of $\tilde{r} = r - 1/(3\tau)$, we can transform (B 2) into

$$\tilde{r}^3 - \frac{1}{3\tau^2}\tilde{r} + \frac{1}{\tau}\left(1 - \frac{2}{27\tau^2} \right) = 0. \qquad \text{(B 3)}$$

Following the general theory for the solution of cubic equations, the solutions for $\tilde{r}$ can now be written as

$$\tilde{r}_k = \frac{2}{3|\tau|}\cos\left[\frac{1}{3}\arccos\left(\text{Sgn}(\tau)\left(1 - \frac{27}{2}\tau^2 \right) \right) - \frac{2\pi k}{3} \right] \quad \text{for } k = 1, 2, 3, \quad \text{(B 4)}$$

and hence

$$r_k = \frac{1}{3\tau} + \frac{2}{3|\tau|}\cos\left[\frac{1}{3}\arccos\left(\text{Sgn}(\tau)\left(1 - \frac{27}{2}\tau^2 \right) \right) - \frac{2\pi k}{3} \right] \quad \text{for } k = 1, 2, 3. \quad \text{(B 5)}$$

The choice of k is now determined by the requirement that $r_k \to 1$ in the limit of vanishing τ (i.e. for infinitesimally small streamline deformation). For $\tau > 0$ (respectively, $\tau < 0$), we find that the only acceptable solution is the one corresponding to $k = 1$ (respectively, $k = 3$). In both cases, the streamline can be parametrized

explicitly, up to the leading order in τ, as

$$r = 1 + \frac{\tau}{2} + O(p^2) = 1 + \frac{1}{3}p\cos\theta + O(p^2) = F(\theta). \tag{B 6}$$

We now compute the surface area $\mathscr{S}$ of a small annular-like region of relative thickness $\delta \ll 1$. We may write

$$\mathscr{S} \approx \int_{\theta=0}^{2\pi} \int_{r=(1-\delta)F(\theta)}^{F(\theta)} r\,\mathrm{d}r\,\mathrm{d}\theta \approx 2\pi\delta(1 + O(p^2) + O(\delta) + O(\delta p^2)). \tag{B 7}$$

Appendix C. Viscous dissipation rate of the basic flow

In this appendix, we derive a simple model to estimate the viscous dissipation of the laminar base flow based on the boundary-layer theory of Wang (1970). Since, on average, the flow is steady, the mean viscous dissipation $\overline{\mathscr{D}_v^L}$ should be equal to the time-averaged power of the Poincaré force (sometimes called Euler force, see e.g. Eckart (1960)), i.e.

$$\overline{\mathscr{D}_v^L} = \overline{\iint \boldsymbol{u} \cdot \left(\boldsymbol{r} \times \frac{\mathrm{d}\gamma}{\mathrm{d}t}\boldsymbol{e}_z \right) \mathrm{d}\boldsymbol{r}}, \tag{C 1}$$

where γ is given by $1 - \varepsilon\cos(\omega t)$ (see §2.1). Since $\omega \gg \sqrt{E}$, we may adapt the local tangential boundary-layer correction provided by Wang (1970) to account for the non-circular shape of the container. It can be expressed in the librating frame as follows:

$$\boldsymbol{u} = \varepsilon \left[\exp\left(\frac{r - F(\theta)}{\delta} \right) \cos\left(\omega t - \frac{r - F(\theta)}{\delta} \right) \right] \boldsymbol{e}_T - \varepsilon\cos(\omega t)\,\boldsymbol{e}_\theta. \tag{C 2}$$

Here, $\boldsymbol{e}_T$ is a unit vector tangential to the streamline, $F(\theta)$ is a parametrization of the boundary (see appendix B for the particular case $n = 3$), which can be approximated by $F(\theta) = 1 + pn^{-1}\cos(n\theta) + O(p^2)$ in the limit $p \ll 1$, and the last term in this expression comes from our librating frame. As such, we obtain

$$\overline{\mathscr{D}_v^L} = \frac{\pi}{\sqrt{2}}\varepsilon^2\sqrt{E\omega}\,[1 - 2\delta + \delta^2(1 + \mathrm{e}^{-\delta^{-1}}(\sin\delta^{-1} - \cos\delta^{-1})) + O(p^2)]. \tag{C 3}$$

Given that n is not present in (C 3), the viscous dissipation rate of the basic flow is independent of n in the limit of small deformation.

In order to verify (C 3), we have performed extensive 2D numerical simulations of the basic flow in which the four parameters ε, p, E and ω are independently varied. The results of this survey are shown in figure 19 and confirm indeed that $\overline{\mathscr{D}_v^L}$ scales, to the leading order, as $\overline{\mathscr{D}_v^L} \sim \sqrt{E\omega}\,\varepsilon^2$. The slope of the dashed line in this figure is approximately 2.13, which is close to the leading-order coefficient $\pi/\sqrt{2} \approx 2.22$ (difference of 4%).

In figure 19(b), we show the dependence of $\overline{\mathscr{D}_v^L}$ on p. Performing a fourth-order polynomial fit to these data points, we obtain $\overline{\mathscr{D}_v^L} = 0.082\,46 - 0.001\,46\,p + 0.027\,p^2 + O(p^3)$. We see that the prefactor in front of the linear term is almost two orders of magnitude smaller than those in front of the constant and quadratic term. The magnitude of this coefficient reduces further when we increase the order of the polynomial fit. This indicates that the first higher-order term in p in (C 3) is indeed
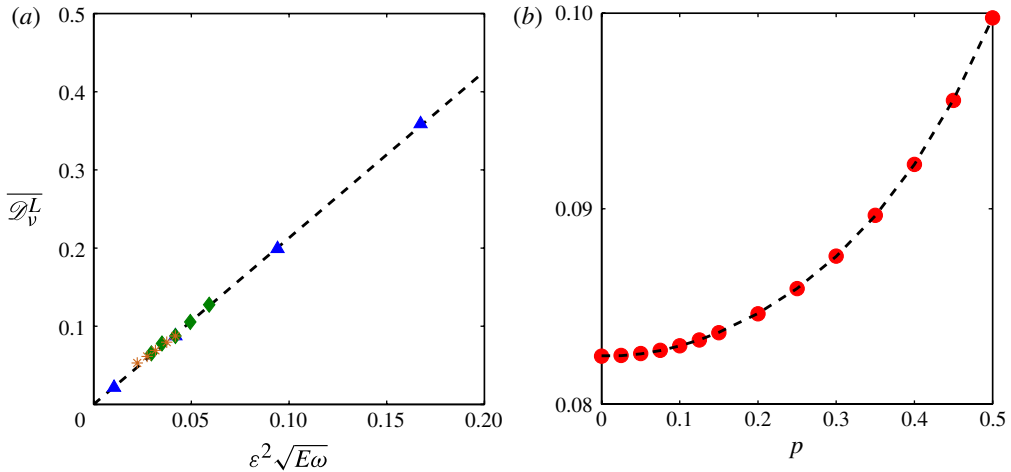
FIGURE 19. (Colour online) Viscous dissipation rate $\overline{\mathscr{D}_v^L}$ of the two-dimensional basic flow for $n = 3$. (*a*) As a function of ε, E and ω with fixed $p = 0.3$. Triangles: varying ε, fixed $E = 5 \times 10^{-4}$ and $\omega = 3.5$. Diamonds: varying E for fixed $\varepsilon = 1$ and $\omega = 3.5$. Asterisks: varying ω for fixed $\varepsilon = 1$ and $E = 5 \times 10^{-4}$. Dashed line: linear fit to the data points, giving a slope of 2.13. (*b*) As a function of p for fixed $E = 5 \times 10^{-4}$, $\varepsilon = 1$ and $\omega = 3.5$. Circles: numerical data points. Dashed line: fourth-order polynomial fit to the data points.

quadratic in p. The constant factor $0.082\,46$ can be compared with the prefactor in (C 3), i.e. $\pi\sqrt{E\omega/2} = 0.092\,929$ (difference of 11 %).

REFERENCES

ABRAMOWITZ, M. & STEGUN, I. A. 1964 *Handbook of Mathematical Functions*, 5th edn. Dover.

ALDRIDGE, K. D. 1967 An experimental study of axisymmetric inertial oscillations of a rotating liquid sphere. PhD thesis, University of Toronto, Canada.

ALDRIDGE, K. D. 1975 Inertial waves and Earth's outer core. *Geophys. J. R. Astron. Soc.* **42** (2), 337–345.

ALDRIDGE, K. D. & TOOMRE, A. 1969 Axisymmetric inertial oscillations of a fluid in a rotating spherical container. *J. Fluid Mech.* **37** (2), 307–323.

BAYLY, B. J. 1986 Three-dimensional instability of elliptical flow. *Phys. Rev. Lett.* **57** (17), 2160–2163.

BAYLY, B. J., HOLM, D. D. & LIFSCHITZ, A. 1996 Three-dimensional stability of elliptical vortex columns in external strain flows. *Phil. Trans. R. Soc. Lond.* A **354** (1709), 895–926.

BENDER, C. M. & ORSZAG, S. A. 1978 *Advanced Mathematical Methods for Scientists and Engineers: Asymptotic Methods and Perturbation Theory*, vol. 1, Springer.

BUSSE, F. H. 2010a Mean zonal flows generated by librations of a rotating spherical cavity. *J. Fluid Mech.* **650**, 505–512.

BUSSE, F. H. 2010b Zonal flow induced by longitudinal librations of a rotating cylindrical cavity. *Physica* D: *Nonlinear Phenom.* **240** (2), 208–211.

CALKINS, M. A., NOIR, J., ELDREDGE, J. D. & AURNOU, J. M. 2010 Axisymmetric simulations of libration-driven fluid dynamics in a spherical shell geometry. *Phys. Fluids* **22**, 086602.

CAMBON, C., BENOIT, J. P., SHAO, L. & JACQUIN, L. 1994 Stability analysis and large-eddy simulation of rotating turbulence with organized eddies. *J. Fluid Mech.* **278**, 175–200.

CAMBON, C., TEISSEDRE, C. & JEANDEL, D. 1985 Étude d'effets couplés de déformation et de rotation sur une turbulence homogène. *J Méc. Théor. Appl.* **4** (5), 629–657.

CÉBRON, D., LE BARS, M., LEONTINI, J., MAUBERT, P. & LE GAL, P. 2010a A systematic numerical study of the tidal instability in a rotating triaxial ellipsoid. *Phys. Earth Planet. Inter.* **182**, 119–128.

CÉBRON, D., LE BARS, M., MAUBERT, P. & LE GAL, P. 2012a Magnetohydrodynamic simulations of the elliptical instability in triaxial ellipsoids. *Geophys. Astrophys. Fluid Dyn.* **106** (4–5), 524–546.

CÉBRON, D., LE BARS, M. & MEUNIER, P. 2010b Tilt-over mode in a precessing triaxial ellipsoid. *Phys. Fluids* **22**, 116601.

CÉBRON, D., LE BARS, M., MOUTOU, C. & LE GAL, P. 2012b Elliptical instability in terrestrial planets and moons. *Astron. Astrophys.* **539** (A78), 1–16.

CÉBRON, D., LE BARS, M., NOIR, J. & AURNOU, J. M. 2012c Libration driven instability. *Phys. Fluids* **24** (6), 061703.

CÉBRON, D., MAUBERT, P. & LE BARS, M. 2010c Tidal instability in a rotating and differentially heated ellipsoidal shell. *Geophys. J. Intl* **182**, 1311–1318.

COMSTOCK, R. L. & BILLS, B. G. 2003 A solar system survey of forced librations in longitude. *J. Geophys. Res.* **108** (E9), 5100, 1–13.

CRAIK, A. D. D. & CRIMINALE, W. O. 1986 Evolution of wavelike disturbances in shear flows: a class of exact solutions of the Navier–Stokes equations. *Proc. R. Soc. Lond.* A **406** (1830), 13–26.

ECKART, C. 1960 *Hydrodynamics of Atmospheres and Oceans*. Pergamon.

ELOY, C. & LE DIZÈS, S. 2001 Stability of the Rankine vortex in a multipolar strain field. *Phys. Fluids* **13**, 660–676.

ELOY, C., LE GAL, P. & LE DIZÈS, S. 2000 Experimental study of the multipolar vortex instability. *Phys. Rev. Lett.* **85** (16), 3400–3403.

ELOY, C., LE GAL, P. & LE DIZÈS, S. 2003 Elliptic and triangular instabilities in rotating cylinders. *J. Fluid Mech.* **476**, 357–388.

FRIEDLANDER, S. & VISHIK, M. M. 1991 Instability criteria for the flow of an inviscid incompressible fluid. *Phys. Rev. Lett.* **66** (17), 2204–2206.

GLEDZER, E. B. & PONOMAREV, V. M. 1992 Instability of bounded flows with elliptical streamlines. *J. Fluid Mech.* **240** (1), 1–30.

GUIMBARD, D., LE DIZÈS, S., LE BARS, M., LE GAL, P. & LEBLANC, S. 2010 Elliptic instability of a stratified fluid in a rotating cylinder. *J. Fluid Mech.* **660**, 240–257.

HAM, F., MATTSSON, K. & IACCARINO, G. 2006 Accurate and stable finite volume operators for unstructured flow solvers. In *Annual Research Briefs*. Center for Turbulence Research, Stanford University, USA.

HENSON, V. E. & MEIER YANG, U. 2000 BoomerAMG: a parallel algebraic multigrid solver and preconditioner. *Appl. Numer. Maths* **41**, 155–177.

HERREMAN, W., CEBRON, D., LE DIZÈS, S. & LE GAL, P. 2010 Elliptical instability in rotating cylinders: liquid metal experiments under imposed magnetic field. *J. Fluid Mech.* **661**, 130–158.

HERREMAN, W., LE BARS, M. & LE GAL, P. 2009 On the effects of an imposed magnetic field on the elliptical instability in rotating spheroids. *Phys. Fluids* **21**, 046602.

KERSWELL, R. R. 1993a Elliptical instabilities of stratified, hydromagnetic waves. *Geophys. Astrophys. Fluid Dyn.* **71** (1), 105–143.

KERSWELL, R. R. 1993b The instability of precessing flow. *Geophys. Astrophys. Fluid Dyn.* **72** (1), 107–144.

KERSWELL, R. R. 2002 Elliptical instability. *Annu. Rev. Fluid Mech.* **34** (1), 83–113.

KERSWELL, R. R. & BARENGHI, C. F. 1995 On the viscous decay rates of inertial waves in a rotating circular cylinder. *J. Fluid Mech.* **285**, 203–214.

KERSWELL, R. R. & MALKUS, W. V. R. 1998 Tidal instability as the source for Io's magnetic signature. *Geophys. Res. Lett.* **25** (5), 603–606.

KEVORKIAN, J. & COLE, J. D. 1996 *Multiple Scale and Singular Perturbation Methods*, vol. 114, Springer.

KIM, J. & MOIN, P. 1985 Application of a fractional-step method to the incompressible Navier–Stokes equation. *J. Comput. Phys.* **59**, 308–323.

LACAZE, L., LE GAL, P. & LE DIZÈS, S. 2004 Elliptical instability in a rotating spheroid. *J. Fluid Mech.* **505**, 1–22.

LACAZE, L., LE GAL, P. & LE DIZÈS, S. 2005 Elliptical instability of the flow in a rotating shell. *Phys. Earth Planet. Inter.* **151** (3–4), 194–205.

LAGRANGE, R., MEUNIER, P., NADAL, F. & ELOY, C. 2011 Precessional instability of a fluid cylinder. *J. Fluid Mech.* **666**, 104–145.

LANDMAN, M. J. & SAFFMAN, P. G. 1987 The three-dimensional instability of strained vortices in a viscous fluid. *Phys. Fluids* **30**, 2339.

LAVOREL, G. & LE BARS, M. 2010 Experimental study of the interaction between convective and elliptical instabilities. *Phys. Fluids* **22**, 114101.

LE BARS, M., LACAZE, L., LE DIZÈS, S., LE GAL, P. & RIEUTORD, M. 2010 Tidal instability in stellar and planetary binary systems. *Phys. Earth Planet. Inter.* **178** (1–2), 48–55.

LE BARS, M., LE DIZÈS, S. & LE GAL, P. 2007 Coriolis effects on the elliptical instability in cylindrical and spherical rotating containers. *J. Fluid Mech.* **585**, 323–342.

LE BARS, M., WIECZOREK, M. A., KARATEKIN, Ö, CÉBRON, D. & LANEUVILLE, M. 2011 An impact-driven dynamo for the early moon. *Nature* **479**, 215–218.

LE DIZÈS, S. 2000 Three-dimensional instability of a multipolar vortex in a rotating flow. *Phys. Fluids* **12**, 2762.

LE DIZÈS, S. & ELOY, C. 1999 Short-wavelength instability of a vortex in a multipolar strain field. *Phys. Fluids* **11**, 500.

LEBLANC, S. & CAMBON, C. 1997 On the three-dimensional instabilities of plane flows subjected to Coriolis force. *Phys. Fluids* **9** (5), 1307–1316.

LEBOVITZ, N. R. & LIFSCHITZ, A. 1996 Short-wavelength instabilities of Riemann ellipsoids. *Phil. Trans. R. Soc. Lond.* A **354** (1709), 927–950.

LIFSCHITZ, A. 1994 On the instability of certain motions of an ideal incompressible fluid. *Adv. Appl. Math.* **15** (4), 404–436.

LIFSCHITZ, A. & HAMEIRI, E. 1991 Local stability conditions in fluid dynamics. *Phys. Fluids* A: *Fluid Dyn.* **3**, 2644.

LIFSCHITZ, A. & HAMEIRI, E. 1993 Localized instabilities of vortex rings with swirl. *Commun. Pure Appl. Maths* **46** (10), 1379–1408.

MALKUS, W. V. R. 1989 An experimental study of global instabilities due to the tidal (elliptical) distortion of a rotating elastic cylinder. *Geophys. Astrophys. Fluid Dyn.* **48** (1), 123–134.

MARGOT, J. L., PEALE, S. J., JURGENS, R. F., SLADE, M. A. & HOLIN, I. V. 2007 Large amplitude libration of Mercury reveals a molten core. *Science* **316** (5825), 710–714.

MASON, D. M. & KERSWELL, R. R. 1999 Nonlinear evolution of the elliptical instability: an example of inertial wave breakdown. *J. Fluid Mech.* **396**, 73–108.

MIYAGOSHI, T. & HAMANO, Y. 2013 Magnetic field variation caused by rotational speed change in a magnetohydrodynamic dynamo. *Phys. Rev. Lett.* **111**, 124501.

MOORE, D. W. & SAFFMAN, P. G. 1975 The instability of a straight vortex filament in a strain field. *Proc. R. Soc. Lond.* A **346** (1646), 413–425.

NOIR, J., CALKINS, M. A., LASBLEIS, M., CANTWELL, J. & AURNOU, J. M. 2010 Experimental study of libration-driven zonal flows in a straight cylinder. *Phys. Earth Planet. Inter.* **182** (1–2), 98–106.

NOIR, J., CÉBRON, D., LE BARS, M., SAURET, A. & AURNOU, J. M. 2012 Experimental study of libration-driven zonal flows in non-axisymmetric containers. *Phys. Earth Planet. Inter.* **204/205**, 1–10.

NOIR, J., HEMMERLIN, F., WICHT, J., BACA, S. M. & AURNOU, J. M. 2009 An experimental and numerical study of librationally driven flow in planetary cores and subsurface oceans. *Phys. Earth Planet. Inter.* **173** (1–2), 141–152.

POINCARÉ, R. 1910 Sur la précession des corps déformables. *Bull. Astron.* I **27**, 321–356.

SAURET, A., CÉBRON, D., LE BARS, M. & LE DIZÈS, S. *et al.* 2012 Fluid flows in a librating cylinder. *Phys. Fluids* **24**, 026603.

SAURET, A., CÉBRON, D., MORIZE, C. & LE BARS, M. 2010 Experimental and numerical study of mean zonal flows generated by librations of a rotating spherical cavity. *J. Fluid Mech.* **662** (1), 260–268.

SAURET, A. & LE DIZÈS, S. 2013 Libration-induced mean flow in a spherical shell. *J. Fluid Mech.* **718**, 181–209.

SIPP, D. & JACQUIN, L. 1998 Elliptic instability in two-dimensional flattened Taylor–Green vortices. *Phys. Fluids* **10**, 839–849.

TILGNER, A. 1999 Driven inertial oscillations in spherical shells. *Phys. Rev. E* **59** (2), 1789–1794.

TSAI, C. Y. & WIDNALL, S. E. 1976 The stability of short waves on a straight vortex filament in a weak externally imposed strain field. *J. Fluid Mech.* **73** (4), 721–733.

VANTIEGHEM, S. 2011 Numerical simulations of quasi-static magnetohydrodynamics using an unstructured finite-volume solver: development and applications. PhD thesis, Université Libre de Bruxelles, Belgium.

WALEFFE, F. 1990 On the three-dimensional instability of strained vortices. *Phys. Fluids* A: *Fluid Dyn.* **2**, 76–80.

WANG, C. Y. 1970 Cylindrical tank of fluid oscillating about a state of steady rotation. *J. Fluid Mech.* **41** (3), 581–592.

WIECZOREK, M. A. & LE FEUVRE, M. 2009 Did a large impact reorient the Moon? *Icarus* **200** (2), 358–366.

WILLIAMS, J. G., BOGGS, D. H., YODER, C. F., RATCLIFF, J. T. & DICKEY, J. O. 2001 Lunar rotational dissipation in solid body and molten core. *J. Geophys. Res.* **106** (E11), 27 933–27 968.

WU, C. C. & ROBERTS, P. H. 2013 On a dynamo driven topographically by longitudinal libration. *Geophys. Astrophys. Fluid Dyn.* **107** (1–2), 20–44.

ZHANG, K., LIAO, X. & EARNSHAW, P. 2004 On inertial waves and oscillations in a rapidly rotating spheroid. *J. Fluid Mech.* **504**, 1–40.